日本磁気学会
ISSN 2432-0250
Journal of the Magnetics Society of Japan
Electronic Journal URL: https://www.jstage.jst.go.jp/browse/msjmag

Vol.46 No.3 2022

Journal

JOURNAL OF THE MAGNETICS SOCIETY OF JAPAN

Vol.46 No.3 2022

日本磁気学会

ISSN 2432-0250

HP: http://www.magnetics.jp/ e-mail: msj@bj.wakwak.com

Electronic Journal: http://www.jstage.jst.go.jp/browse/msjmag

Journal of the Magnetics Society of Japan
Vol. 46, No. 3

Electronic Journal URL: https://www.jstage.jst.go.jp/browse/msjmag

CONTENTS

J. Magn. Soc. Jpn., **46**, 49-57 (2022)

<Paper>

Adjacent Track Interference in Heat-Assisted Magnetic Recording

T. Kobayashi, Y. Nakatani*, and Y. Fujiwara

Graduate School of Engineering, Mie Univ., *1577 Kurimamachiya-cho, Tsu 514-8507, Japan*

*Graduate School of Informatics and Engineering, Univ. of Electro-Communications, *1-5-1 Chofugaoka, Chofu 182-8585, Japan*

We examine here the adjacent track interference (ATI) problem that arises when writing in an adjacent track for heat-assisted magnetic recording combined with shingled magnetic recording (shingled HAMR). For ATI, the bit error rate is a function of readout track width. We calculate the bit error rate and the minimum normalized readout field for various readout track widths. The factors affecting ATI are grain temperature and grain volume. We compare ATI and writing sensitivity for all combinations of 2 and 4 Tbpsi, and 6 and 9 grains/bit under the conditions of constant grain volume and constant grain height. For constant grain volume, 4 Tbpsi shingled HAMR is less advantageous than 2 Tbpsi shingled HAMR in terms of ATI due to the higher grain temperature caused by the smaller grain pitch. The grain number per bit must be lower and the grain height must be greater to be able to improve ATI for 4 Tbpsi shingled HAMR. We show there to be a loss of writing sensitivity for 4 Tbpsi shingled HAMR due to a statistical factor caused by the lower grain number per bit and the higher thermal stability factor resulting from the larger grain volume.

Key words: HAMR, ATI, grain temperature, grain volume, grain number, thermal stability factor

1. Introduction

Heat-assisted magnetic recording (HAMR) shows potential as a next-generation magnetic recording method that achieves high recording capacities. HAMR is a recording technique in which the medium is heated to reduce coercivity during the writing period.

Information stability when writing in the adjacent track, namely adjacent track interference (ATI), is an important characteristic for HAMR[1] as well as in conventional magnetic recording.

We have previously examined ATI for 2 Tbpsi and 9 grains/bit HAMR combined with shingled magnetic recording (shingled HAMR). We evaluated the error distribution using the expected value of the magnetization rather than the bit error rate[2], and noted that when the recording layer is thin, ATI worsens, since the grain volume is smaller. ATI worsens as the thermal gradient decreases. Since the thermal gradient decreases as the Curie temperature decreases, ATI worsens as the Curie temperature decreases.

In this paper, we examine ATI on shingled HAMR. With ATI, the bit error rate is a function of readout track width. We calculate here, for various readout track widths, the bit error rate and the minimum normalized readout field that must be readable without error after writing in the adjacent track. ATI and writing sensitivity are compared for all combinations of 2 and 4 Tbpsi, and 6 and 9 grains/bit under the conditions of constant grain volume and constant grain height, since the factors affecting ATI are grain temperature and grain volume.

Corresponding author: T. Kobayashi (e-mail: kobayasi @phen.mie-u.ac.jp).

2. Calculation Method and Conditions

2.1 Magnetic properties

The temperature dependence of the medium magnetization M_s was calculated by employing mean field analysis[3], and that of the medium anisotropy constant K_u was assumed to be proportional to M_s^2 [4]. $M_s(T_c, T)$ is a function of the Curie temperature T_c and temperature T. $M_s(T_c = 770\ \mathrm{K}, T = 300\ \mathrm{K}) = 1000$ emu/cm^3 was assumed for FePt, a potential HAMR medium material due to its large K_u and relatively low T_c. Based on this assumption, the M_s value can be calculated for all values of T_c and T.

We have introduced an HAMR medium parameter, namely, the medium anisotropy constant ratio K_u/K_{bulk}[5] in place of K_u, since the K_u value at the storage temperature is a function of T_c, which is strongly related to the writing property. K_u/K_{bulk} is the intrinsic ratio of the medium K_u to bulk FePt K_u, which is independent of T_c, and is valid for any temperature from zero Kelvin to Curie temperature.

The $K_u(T_c, K_u/K_{bulk}, T)$ value is a function of T_c, K_u/K_{bulk}, and T. $K_u(T_c = 770\ \mathrm{K}, K_u/K_{bulk} = 1, T = 300\ \mathrm{K}) = 70$ Merg/cm^3 was assumed for bulk FePt. Using this assumption, the K_u value can be calculated for all values of T_c, K_u/K_{bulk}, and T. No intrinsic distribution of K_u was assumed. However, there was a fluctuation in K_u caused by T_c variation.

The T_c value can be adjusted by changing the Cu composition z for $(Fe_{0.5}Pt_{0.5})_{1-z}Cu_z$.

2.2 Information stability

We assumed the medium to be granular. One bit has m grains in the cross-track (row i) direction and n grains in the down-track (column j) direction, *i.e.*, there are $m \times n$ grains/bit.

The information stability for ATI was estimated using the grain error probability P[6],

$$P = 1 - \exp\left(-f_0 t \exp\left(-\frac{K_{\mathrm{ueff}}V}{kT}\left(1+\frac{H_{\mathrm{w}}}{H_{\mathrm{keff}}}\right)^2\right)\right), \quad (1)$$
$$(|H_{\mathrm{w}}| < H_{\mathrm{keff}})$$

taking account of the shape anisotropy $M_{\mathrm{s}}H_{\mathrm{d}}/2$ using a self-demagnetizing field H_{d} where f_0, t, K_{ueff}, V, k, T, and H_{w} are respectively the attempt frequency[7], time, the effective anisotropy constant, the grain volume, the Boltzmann constant, the grain temperature while writing in the adjacent track, and the writing field. $K_{\mathrm{ueff}} = K_{\mathrm{u}} - M_{\mathrm{s}}H_{\mathrm{d}}/2$, $H_{\mathrm{d}} = 8M_{\mathrm{s}}\arctan\left(D^2/(h\sqrt{2D^2+h^2})\right)$, $V = D \times D \times h$ where D and h are respectively the grain size and height. However, H_{d} does not affect the results, as reported in a previous paper[8], since $K_{\mathrm{u}} \gg M_{\mathrm{s}}H_{\mathrm{d}}/2$. Therefore, the magnetostatic field from surrounding grains can also be ignored. It was assumed that there is no exchange coupling between grains.

To evaluate the grain error distribution, we calculated the expected value of the magnetization $E[M_{\mathrm{s}}]$,

$$E[M_{\mathrm{s}}] = (1-P)M_{\mathrm{s}} + P(-M_{\mathrm{s}}) = (1-2P)M_{\mathrm{s}}. \quad (2)$$

The $E[M_{\mathrm{s}}]$ value was averaged over one row of grains as

$$E[M_{\mathrm{si}}] = \frac{\sum_{j=1}^{n}(1-2P_{ij})M_{sij}(T_{cij},\ 330\ \mathrm{K})}{n} \quad (3)$$

at a readout temperature of 330 K after writing in the adjacent track, since there is a temperature distribution in the cross-track direction.

The bit error rate bER was also calculated by employing P. For example, for 4 grains/bit, the 1 grain-error bit error rate ${}_4\mathrm{bER}_1$ is expressed as

$${}_4\mathrm{bER}_1 = Er_1P_1(1-P_2)(1-P_3)(1-P_4) + \cdots + Er_4(1-P_1)(1-P_2)(1-P_3)P_4, \quad (4)$$

the 2 grain-error bit error rate ${}_4\mathrm{bER}_2$ as

$${}_4\mathrm{bER}_2 = Er_{12}P_1P_2(1-P_3)(1-P_4) + \cdots + Er_{34}(1-P_1)(1-P_2)P_3P_4, \quad (5)$$

the 3 grain-error bit error rate ${}_4\mathrm{bER}_3$ as

$${}_4\mathrm{bER}_3 = Er_{123}P_1P_2P_3(1-P_4) + \cdots + Er_{234}(1-P_1)P_2P_3P_4, \quad (6)$$

and the 4 grain-error bit error rate ${}_4\mathrm{bER}_4$ as

$${}_4\mathrm{bER}_4 = P_1P_2P_3P_4, \quad (7)$$

where

$$Er_k = 1, \text{ if } \frac{\sum_{i,j}M_{sij}(T_{cij},\ 330\ \mathrm{K})D_{ij}^2}{(m\times n)M_{\mathrm{s}}(T_{\mathrm{cm}},\ 330\ \mathrm{K})D_{\mathrm{m}}^2} \le E_{\mathrm{th}}, \quad (8)$$

and

$$Er_k = 0, \text{ if } \frac{\sum_{i,j}M_{sij}(T_{cij},\ 330\ \mathrm{K})D_{ij}^2}{(m\times n)M_{\mathrm{s}}(T_{\mathrm{cm}},\ 330\ \mathrm{K})D_{\mathrm{m}}^2} > E_{\mathrm{th}}, \quad (9)$$

where T_{cm} and D_{m} are respectively the mean Curie temperature and the mean grain size. Errors occur in some grains of a bit. We assumed that if the ratio of $\sum_{i,j}M_{sij}(T_{cij},\ 330\ \mathrm{K})D_{ij}^2$ to $(m\times n)M_{\mathrm{s}}(T_{\mathrm{cm}},\ 330\ \mathrm{K})D_{\mathrm{m}}^2$ in Eqs. (8) and (9) is greater than the error threshold E_{th}, the bit will be error-free after writing in the adjacent track, where the numerator $\sum_{i,j}M_{sij}(T_{cij},\ 330\ \mathrm{K})D_{ij}^2$ is the surface magnetic charge of the grains that are magnetized in the recording direction, and the denominator $(m\times n)M_{\mathrm{s}}(T_{\mathrm{cm}},\ 330\ \mathrm{K})D_{\mathrm{m}}^2$ is the total surface magnetic charge. M_{sij}, T_{cij}, and D_{ij} are respectively the magnetization, the Curie temperature, and the grain size of the ij-th grain. The total bit error rate ${}_4\mathrm{bER}$ is the summation of each bit error rate ${}_4\mathrm{bER}_k$ as follows

$${}_4\mathrm{bER} = \Sigma_k\ {}_4\mathrm{bER}_k. \quad (10)$$

The calculation bit number was 10^7. The criterion determining whether or not information is stable was assumed to be a bER of 10^{-3}.

The normalized readout field H_0 which is a magnetic field from grains can roughly be represented by E_{th} as

$$H_0 = 2E_{\mathrm{th}} - 1, \quad (11)$$

since E_{th} equals one when almost all grains are magnetized in the recording direction, and equals a half when almost half of grains are magnetized. The minimum normalized readout field, that must be readable without error after writing in the adjacent track, can be estimated by E_{th} to have a bER of 10^{-3}.

2.3 Grain arrangement and temperature

We examined ATI for all combinations of 2 and 4 Tbpsi, and 6 and 9 grains/bit.

Table 1 Calculation conditions for adjacent track interference.

Intergrain spacing Δ_{G} (nm)	1.0
Standard deviation $\sigma_{\mathrm{D}}/D_{\mathrm{m}}$ (%) of D_{m}	15
Standard deviation $\sigma_{\mathrm{Tc}}/T_{\mathrm{cm}}$ (%) of T_{cm}	2
Gilbert damping constant α	0.1
Time t (ns)	1
Thermal gradient $\partial T/\partial y$ (K / nm)	12
Writing field H_{w} (kOe)	−10

The conditions used when calculating the P value are summarized in Table 1. We assumed the intergrain spacing Δ_{G} to be 1.0 nm regardless the grain number per bit and the recording density. The grain size distribution was log-normal with a standard deviation $\sigma_{\mathrm{D}}/D_{\mathrm{m}}$ of 15 % for D_{m}, and the T_{c} distribution was normal with a standard deviation $\sigma_{\mathrm{Tc}}/T_{\mathrm{cm}}$ of 2 % for T_{cm}. The attempt frequency f_0 is a function of the Gilbert damping constant α[7]. We used an α value of 0.1. Time t and the writing field H_{w} were assumed to be 1 ns and −10 kOe, respectively. For simplicity, a

thermal gradient $\partial T/\partial y$ of 12 K/nm was assumed to be uniformly constant in the cross-track direction.

Figures 1 and 2 respectively show the grain arrangement and temperature for 2 and 4 Tbpsi.

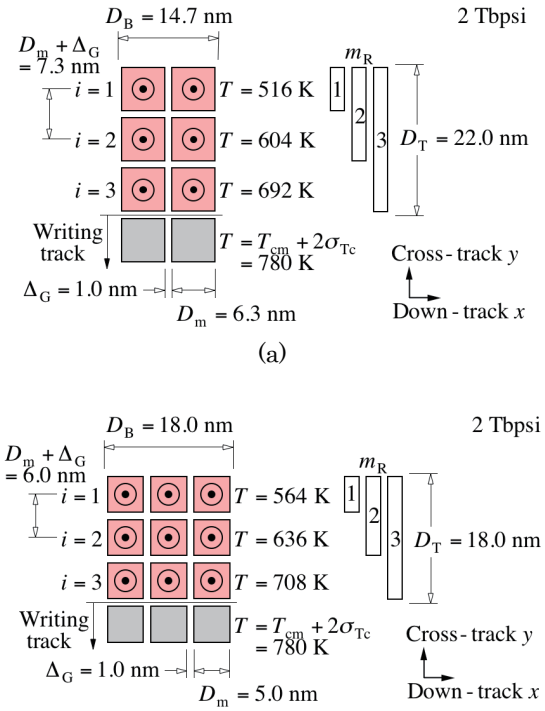

Fig. 1 Grain arrangement and temperature for (a) 6 and (b) 9 grains/bit in 2 Tbpsi shingled HAMR.

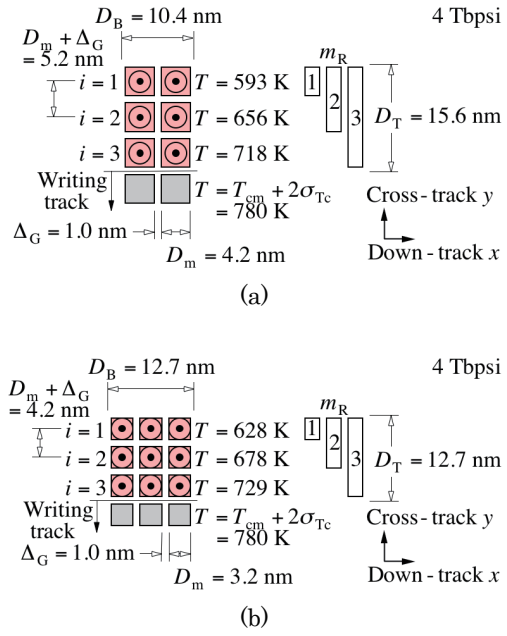

Fig. 2 Grain arrangement and temperature for (a) 6 and (b) 9 grains/bit in 4 Tbpsi shingled HAMR.

The D_m value was determined by

$$D_m = \sqrt{\frac{S}{m \times n}} - \Delta_G, \tag{12}$$

where S is the bit area. The bit aspect ratio is $D_T/D_B = m/n$ where $D_T = m(D_m + \Delta_G)$, $D_B = n(D_m + \Delta_G)$, and $D_m + \Delta_G$ are the track width, the bit length, and the grain pitch, respectively. The bit areas S are 323 and 161 nm^2 for the recording densities of 2 and 4 Tbpsi, respectively.

The writing temperature of the grains at the track edge in the writing track was assumed to be $T_{cm} + 2\sigma_{Tc}$, taking account of σ_{Tc} where T_{cm} = 750 K. Based on this assumption, almost all grains in the writing track are heated to above their Curie temperatures during the writing period.

The bER value is a function of readout track width. We therefore calculated the bER and the H_0 values for readout rows m_R of 1 (i = 1), 2 (i = 1 and 2), and 3 (i = 1, 2, and 3).

2.4 Writing sensitivity

There are various calculation methods for researching HAMR writing properties: micromagnetic calculation using the Landau-Lifshitz-Gilbert (LLG) equation, applying the Landau-Lifshitz-Bloch (LLB) equation, and a model calculation[9] that we have proposed using the Néel-Arrhenius model with Stoner-Wohlfarth grain. The α value at the writing temperature is an important medium parameter. However, the α value and its temperature dependence for FePt near the Curie temperature are not currently known. The reported calculation results using all methods are therefore for reference only. However, they are useful for researching the effects on the writing property of changing the calculation parameters.

We examined the H_w dependence of the signal to noise ratio SNR, employing a micromagnetic calculation using the LLG equation where the magnetic properties used here change with temperature. The temperature dependence was calculated using mean field analysis. We believe that the use of the LLG equation that includes the temperature dependence of magnetic properties is a suitable replacement for the LLB equation. We also examined the H_w dependence of bER using our model calculation, with the aim of grasping the physical implications of the writing property in HAMR.

The grain arrangement and the medium properties are the same as those for the ATI calculation. The α value used here was 0.1 without temperature dependence. The linear velocity v was 10 m/s. For simplicity, the thermal gradients $\partial T/\partial x$ of 12 K/nm and $\partial T/\partial y$ of 0, respectively, were assumed to be uniform in both the down-track and cross-track directions. The writing field was assumed to be spatially uniform, the direction to be perpendicular to the medium plane, the recording frequency to be $v/(2D_B)$, and the rise time to

be zero. The demagnetizing field was included, but the magnetostatic field during writing was neglected.

In the LLG calculation, the output signal, media noise, and media SNR were calculated using a sensitivity function[10], which is the same as the cross-track width of the simulation region, a magnetoresistive read head with a 15 nm shield-shield spacing, and a 4.0 nm head-medium spacing for 2 Tbpsi and 6 grains/bit shingled HAMR with D_B of 14.7 nm. Since the SNR value is also affected by the resolution of the read head, we changed the shield-shield spacing to $(D_B/14.7) \times 15$ nm for other calculations. We used a pattern consisting of 1536 grains for the down-track direction, and we used 32 patterns for the SNR calculation.

In the model calculation, the resolution corresponds to infinity. The calculation bit number was 10^6.

3. Calculation Results

3.1 Constant grain volume

The factors affecting ATI are
(1) grain temperature T in effective thermal stability factor $K_{ueff}(T)V/(kT)$, and
(2) grain volume V in $K_{ueff}V/(kT)$.

The T value for a small grain number per bit and/or a low recording density is easy to reduce, since the grain pitch $D_m + \Delta_G$ increases.

The V value is also easy to increase, since the grain area D_m^2 increases.

We first examined ATI under the condition of constant grain volume V of 110 nm^3. This condition is summarized in Table 2 for 2 and 4 Tbpsi, and $m \times n$ = 3×2 = 6 and 3×3 = 9 grains/bit.

Table 2 Calculation conditions under the condition of constant grain volume V = 110 nm^3.

Recording density (Tbpsi)	2	2	4	4
$m \times n$ (grains / bit)	3×2	3×3	3×2	3×3
D_m (nm)	6.3	5.0	4.2	3.2
h (nm)	2.7	4.4	6.3	10.5
h / D_m	0.43	0.89	1.5	3.2
V (nm^3)	110	110	110	110
D_B (nm)	14.7	18.0	10.4	12.7
D_T (nm)	22.0	18.0	15.6	12.7
D_T / D_B	1.5	1.0	1.5	1.0
T_{cm} (K)	750	750	750	750
K_u / K_{bulk}	0.8	0.8	0.8	0.8
$K_{ueff}V/(kT)$ (T = 350 K)	105	109	111	113

The grain height (recording layer thickness) h for 4 Tbpsi and 9 grains/bit was assumed to be 10.5 nm. The grain aspect ratio h/D_m is therefore relatively large at 3.2 and the $K_{ueff}V/(kT)$ value rises to a high value of 113, which is sufficiently large for 10 years of archiving[8]. The h/D_m value decreases as the grain number per bit and/or the recording density decreases. The h and h/D_m values for 2 Tbpsi and 6 grains/bit are only 2.7 nm and 0.43, respectively, and the $K_{ueff}V/(kT)$ value is 105, which is slightly smaller than 113 due to shape anisotropy.

Figure 3 (a) shows the number of bits plotted against the expected value of magnetization $E[M_{si}]$ averaged over one-row grains after writing in the adjacent track for 4 Tbpsi and 9 grains/bit. It also shows the grain error distribution. The negative $E[M_{si}]$ represents more than half of 3 grains errors, since the number of one-row grains n is three. The peaks in the figure represent grain error for the grains with the mean Curie temperature. The grain error increases in the order of the 1st (i = 1), 2nd (i = 2), and 3rd (i = 3) rows, since the temperature increases in this order. Significant information degradation can be seen even in the 2nd (i = 2) row grains.

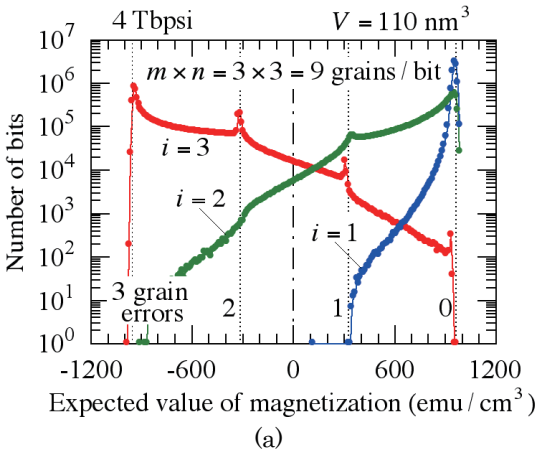

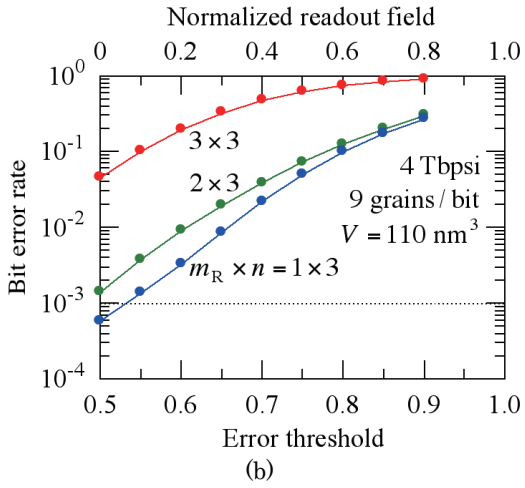

Fig. 3 (a) Number of bits plotted against expected value of magnetization $E[M_{si}]$ and (b) bit error rate as a function of error threshold E_{th} and normalized readout field H_0 after writing in adjacent track in 4 Tbpsi and 9 grains/bit shingled HAMR.

The bER value as a function of E_{th} for various readout rows m_R is shown in Fig. 3 (b). The second horizontal axis is the H_0 value estimated using Eq. (11). The

readout grain numbers are $m_R \times n = 1 \times 3 = 3$, $2 \times 3 = 6$, and $3 \times 3 = 9$ grains for m_R of 1, 2, and 3, respectively. With no ATI, the bER declines with increasing readout grain number, since the probability of a simultaneous error is statistically low. On the other hand, the grain temperature increases in the order of the 1st ($i = 1$), 2nd ($i = 2$), and 3rd ($i = 3$) rows. As a result, the bER value increases as the m_R value increases. There is no H_0 greater than 0 that satisfies bER of 10^{-3} for m_R of 2 and 3.

The row-grain temperature dependence of bER for m_R of 1 in 2 Tbpsi is shown in Fig. 4 (a), and that in 4 Tbpsi is shown in Fig. 5 (a). The inserted scale indicates the grain temperature at the 1st ($i = 1$), 2nd ($i = 2$), and 3rd ($i = 3$) rows as shown in Figs. 1 and 2. Although the grain volumes are the same, the bER value for 6 grains/bit (2 readout grains) is larger than that for 9 grains/bit (3 readout grains) due to a statistical factor. The bER values for 2 and 4 Tbpsi are almost the same, as shown in Figs. 4 (a) and 5 (a), since the grain volumes are the same. However, the grain temperature for 2 Tbpsi is clearly lower than that for 4 Tbpsi due to the larger grain pitch.

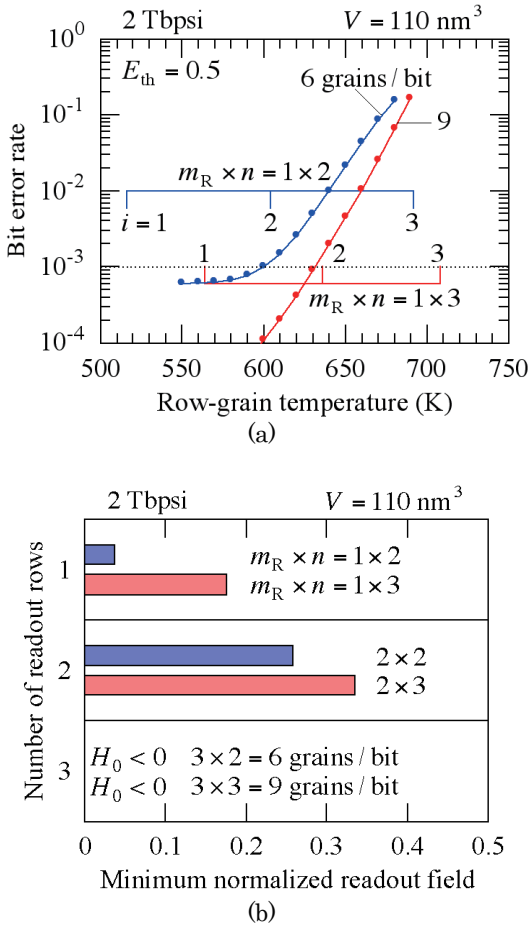

Fig. 4 (a) Row-grain temperature dependence of bit error rate and (b) minimum normalized readout field H_0 for various numbers of readout rows m_R under the condition of constant grain volume $V = 110$ nm^3 in 2 Tbpsi shingled HAMR.

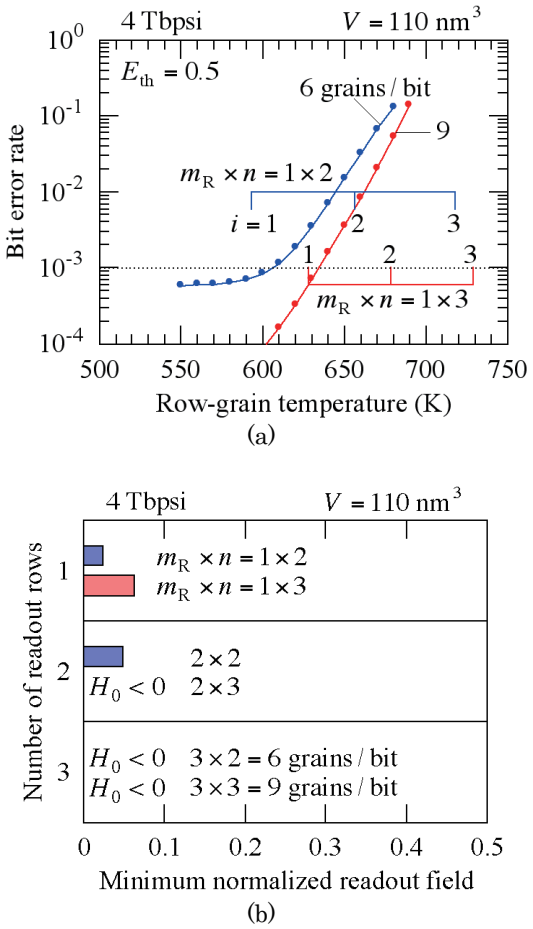

Fig. 5 (a) Row-grain temperature dependence of bit error rate and (b) minimum normalized readout field H_0 for various numbers of readout rows m_R under the condition of constant grain volume $V = 110$ nm^3 in 4 Tbpsi shingled HAMR.

As the temperature decreases, the bER value for 6 grains/bit tends to saturate. When the temperature is sufficiently low, errors are caused by clusters of small grains. The grain number per bit may increase at that time, and the bER value may be lower. This problem is a subject for future study.

Figures 4 (b) and 5 (b) respectively show the minimum normalized readout field H_0 for various numbers of readout rows m_R in 2 and 4 Tbpsi. The temperature at the 1st row ($i = 1$) is obviously lower than that at the 2nd row ($i = 2$). However, Fig. 4 (b) shows the H_0 value for m_R of 2 ($i = 1$ and 2) to be greater than that for m_R of 1 ($i = 1$) for a statistical reason. The H_0 values for 2 Tbpsi are considerably larger than those for 4 Tbpsi, as shown in Figs. 4 (b) and 5 (b) due to the lower grain temperature, as shown in Figs. 4 (a) and 5 (a).

The temperature difference between 6 and 9 grains/bit or 2 and 4 Tbpsi is relatively small. However, ATI is markedly affected by this difference, since temperature is a strongly impacting parameter. Temperature T is related to the effective anisotropy constant $K_{ueff}(T)$ and the denominator T in the effective thermal stability factor $K_{ueff}(T)V/(kT)$, and $K_{ueff}(T)V/(kT)$ is a variable

in the exponential function shown in Eq. (1) when calculating the grain error probability.

The above results are confirmed by the results illustrated in Figs. 6 and 7, which show the number of bits against $E[M_{si}]$ in 2 (9 grains/bit) and 4 (6 grains/bit) Tbpsi, respectively. The grain error distribution for 4 Tbpsi and 6 grains/bit is worse than that for 2 Tbpsi and 9 grains/bit.

These results show that, assuming constant grain volume, 4 Tbpsi shingled HAMR has a disadvantage over 2 Tbpsi shingled HAMR in terms of ATI due to the higher grain temperature caused by the smaller grain pitch.

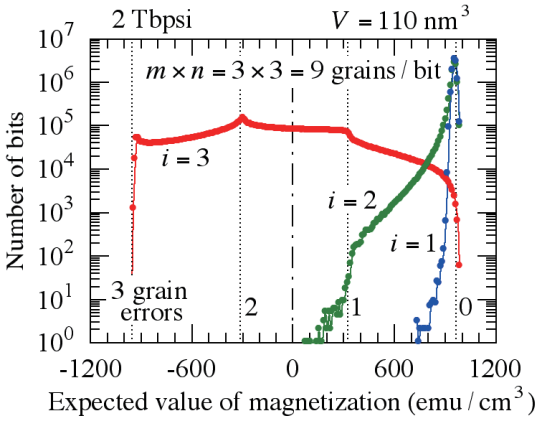

Fig. 6 Number of bits plotted against expected value of magnetization $E[M_{si}]$ for V = 110 nm^3 in 2 Tbpsi and 9 grains/bit shingled HAMR.

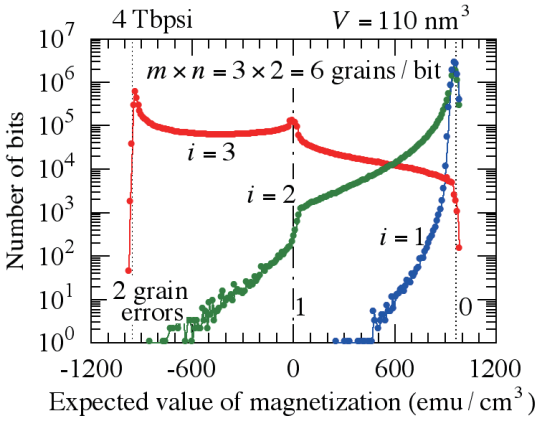

Fig. 7 Number of bits plotted against expected value of magnetization $E[M_{si}]$ for V = 110 nm^3 in 4 Tbpsi and 6 grains/bit shingled HAMR.

Figure 8 shows the writing field H_w dependence of (a) SNR calculated using the LLG equation and (b) bER using our model for 2 and 4 Tbpsi, and 6 and 9 grains/bit. Since HAMR requires the medium to be heated to reduce coercivity at the time of writing, the coercivity of the medium can be reduced by any amount. However, as explained below, a relatively large H_w is necessary.

The information stability for 10 years of archiving has been discussed employing the Néel-Arrhenius model with Stoner-Wohlfarth grain,

$$f_0 t \exp\left(-\frac{K_{ueff}V}{kT}\right). \quad (13)$$

The Néel-Arrhenius model is valid for any time from the picosecond order to more than 10 years, since the attempt period $1/f_0$ has a value in picoseconds for the HAMR granular medium. The information stability for 10 years of archiving is extrapolated as a stack of phenomena in picoseconds. We therefore believe that the Néel-Arrhenius model is valid for analysis of the HAMR writing process. In fact, our model calculation using this model can almost entirely explain the results of LLG simulation as shown in a previous paper[9] and as shown in Fig. 8. In our model, the Boltzmann factor,

$$\exp\left(-\frac{K_{ueff}V}{kT}\left(1+\frac{H_w}{H_{keff}}\right)^2\right), \quad (14)$$

in the Néel-Arrhenius model is interpreted as a grain-magnetization reversal probability for each attempt, and the writing property of HAMR can be understood in terms of the Boltzmann factor and f_0 during the writing period.

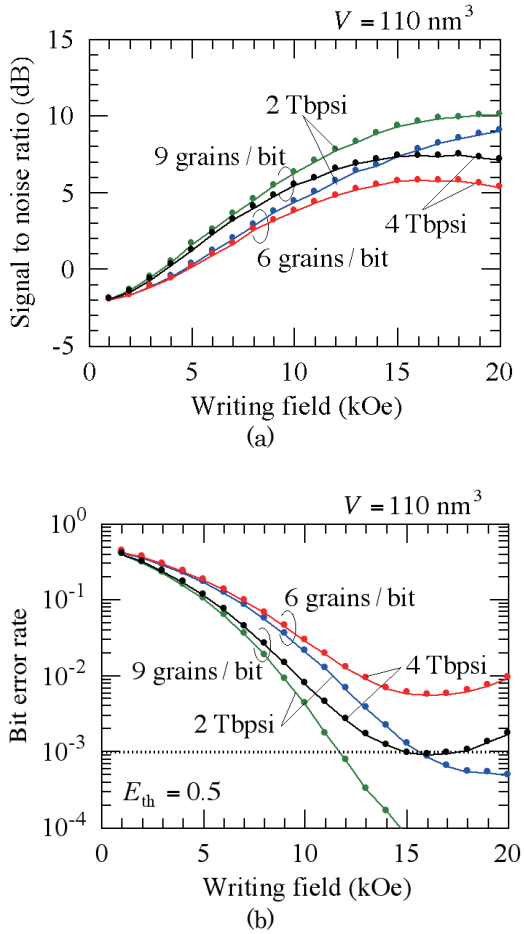

Fig. 8 Writing field dependence of (a) signal to noise ratio and (b) bit error rate under the condition of constant grain volume V = 110 nm^3 in 2 and 4 Tbpsi, and 6 and 9 grains/bit shingled HAMR.

Although the Boltzmann factor approaches unity at near T_c, f_0 falls to a small value[7]. The opportunity for magnetization reversal in the recording direction is small. Although the f_0 value rises at a temperature slightly lower than T_c, the Boltzmann factor falls to a low value. The likelihood of magnetization reversal is thus low. A relatively large $|H_w|$ value ($H_w < 0$) is needed for the Boltzmann factor to increase. Therefore, the reason that a relatively large H_w is required in HAMR is that the writing sensitivity is determined not by the coercivity but by the thermal stability factor modified by H_w,

$$\frac{K_{ueff}V}{kT}\left(1+\frac{H_w}{H_{keff}}\right)^2. \quad (15)$$

Figure 8 shows that if the grain numbers per bit are the same, the writing sensitivities are almost the same for 2 and 4 Tbpsi in the relatively small H_w region in which normal write-error (WE) is dominant. WE results from the magnetization not switching in the recording direction, and occurs during writing. WE affects all the grains in a bit. The Boltzmann factor during the writing period is a key factor in WE[9]. Since the grain volumes are the same, the Boltzmann factors are also almost the same. Therefore, if the grain numbers per bit are the same, the writing sensitivities are almost the same. For a statistical reason, the SNR value for 6 grains/bit is smaller than that for 9 grains/bit, which means that the writing sensitivity for 6 grains/bit is worse than that for 9 grains/bit.

On the other hand, the SNR values for 4 Tbpsi are smaller than those for 2 Tbpsi in the relatively large H_w region in which the influence of erasure-after-write (EAW) is strongly evident. EAW consists of grain magnetization reversal in the opposite direction to the recording direction. This is caused by the change in writing field direction at the end of the writing time. EAW thus occurs after writing. EAW affects the grains at the bit boundary. The Boltzmann factor at the end of the writing time is a key factor in EAW[9]. Since the Boltzmann factor increases as the $|H_w|$ value ($H_w < 0$) increases, EAW is strongly evident in relatively large H_w regions. EAW also occurs more in 4 Tbpsi due to the higher grain temperature caused by the smaller bit length.

3.2 Constant grain height

Next, since ATI is worse in 4 Tbpsi shingled HAMR, we examined ATI under the condition of constant grain height h of 10.5 nm. This condition is summarized in Table 3 for 2 and 4 Tbpsi, and $m \times n = 3 \times 2 = 6$ and $3 \times 3 = 9$ grains/bit.

The $K_{ueff}V/(kT)$ value reaches to 267 for 2 Tbpsi and 9 grains/bit. As mentioned below, this large $K_{ueff}V/(kT)$ value is very useful in reducing ATI.

Table 3 Calculation conditions under the condition of constant grain height h = 10.5 nm.

Recording density (Tbpsi)	2	2	4	4
$m \times n$ (grains / bit)	3 × 2	3 × 3	3 × 2	3 × 3
D_m (nm)	6.3	5.0	4.2	3.2
h (nm)	10.5	10.5	10.5	10.5
h / D_m	1.7	2.1	2.5	3.2
V (nm^3)	421	261	184	110
D_B (nm)	14.7	18.0	10.4	12.7
D_T (nm)	22.0	18.0	15.6	12.7
D_T / D_B	1.5	1.0	1.5	1.0
T_{cm} (K)	750	750	750	750
K_u / K_{bulk}	0.8	0.8	0.8	0.8
$K_{ueff}V / (kT)$ (T = 350 K)	427	267	188	113

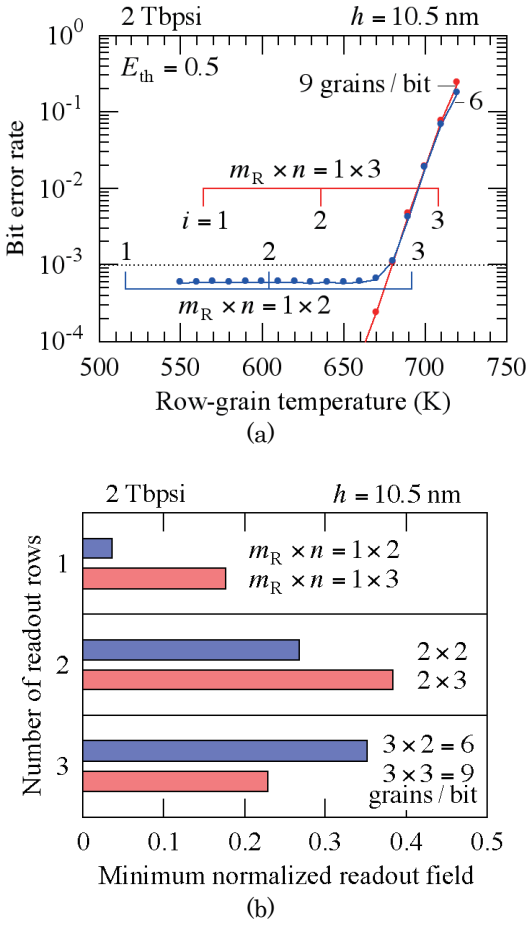

Fig. 9 (a) Row-grain temperature dependence of bit error rate and (b) minimum normalized readout field H_0 for various numbers of readout rows m_R under the condition of constant grain height h = 10.5 nm in 2 Tbpsi shingled HAMR.

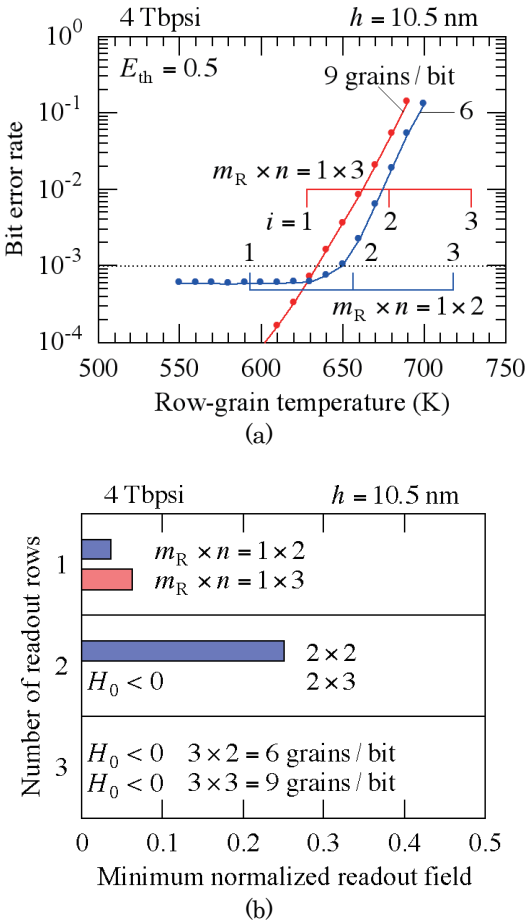

Fig. 10 (a) Row-grain temperature dependence of bit error rate and (b) minimum normalized readout field H_0 for various numbers of readout rows m_R under the condition of constant grain height h = 10.5 nm in 4 Tbpsi shingled HAMR.

The row-grain temperature dependence of bER for m_R of 1 in 2 Tbpsi is shown in Fig. 9 (a). The bER values for 6 and 9 grains/bit are almost the same for temperatures above 680 K. Figures 9 (b) shows the minimum H_0 for various numbers of readout rows m_R. The H_0 value for 9 grains/bit is very large for m_R of 2, since the bER value is sufficiently small at the 1st and 2nd rows, as shown in Fig. 9 (a), due to the large $K_{ueff}V/(kT)$ value, and since the grain number is large.

In contrast, Fig. 10 (a) shows the row-grain temperature dependence of bER for m_R of 1 in 4 Tbpsi. The bER value for 6 grains/bit in Fig. 10 (a) becomes smaller than that for 6 grains/bit in Fig. 5 (a) when the h value was increased to 10.5 from 6.3 nm. The bER value for 6 grains/bit becomes smaller than that for 9 grains/bit for temperatures above 630 K, due to the larger grain volume. Therefore, the H_0 value for 6 grains/bit is relatively large for m_R of 2, as shown in Fig. 10 (b).

The above results are confirmed by the results shown in Figs. 11 and 12, which respectively show the number of bits against $E[M_{si}]$ in 2 (9 grains/bit) and 4 (6 grains/bit) Tbpsi. No errors can be seen in the 1st (i = 1), 2nd (i = 2) rows for 2 Tbpsi, as shown in Fig. 11. On the other hand, there is a clear error in the 2nd (i = 2) row for 4 Tbpsi, as shown in Fig. 12.

As a result, ATI was improved as shown in Figs. 6 and 11 after the h value was increased from 4.4 to 10.5 nm for 2 Tbpsi and 9 grains/bit, and as shown in Figs. 7 and 12 from 6.3 to 10.5 nm for 4 Tbpsi and 6 grains/bit. Although a larger h/D_m is necessary to improve ATI, the larger h/D_m value appears to make it too difficult to manufacture a recording layer.

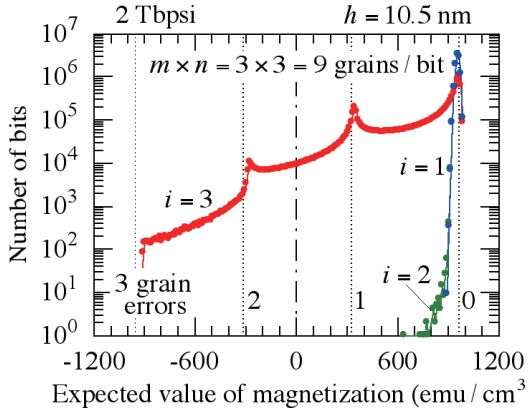

Fig. 11 Number of bits plotted against expected value of magnetization $E[M_{si}]$ for h = 10.5 nm in 2 Tbpsi and 9 grains/bit shingled HAMR.

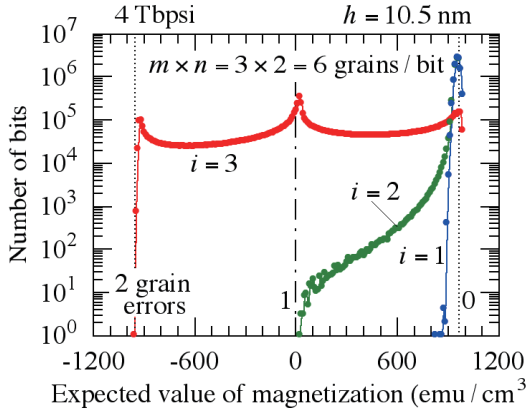

Fig. 12 Number of bits plotted against expected value of magnetization $E[M_{si}]$ for h = 10.5 nm in 4 Tbpsi and 6 grains/bit shingled HAMR.

Even if the larger h/D_m value can be achieved, the writing sensitivity is expected to be worse. The improvement in ATI indicates a deterioration in writing sensitivity, since ATI means writing in the adjacent track. Figure 13 shows the H_w dependence of (a) SNR and (b) bER for 2 and 4 Tbpsi, and 6 and 9 grains/bit. The reason for the difference in writing sensitivity between [2 Tbpsi, 9 grains/bit, h = 4.4 nm] seen in Fig. 8 and [2 Tbpsi, 9 grains/bit, h = 10.5 nm] seen in Fig. 13 is the difference in grain volume. The difference in writing sensitivity between [4 Tbpsi, 6 grains/bit, h = 6.3 nm] and [4 Tbpsi, 6 grains/bit, h = 10.5 nm] is also due the difference in grain volume. As expected, the

writing sensitivity worsens as the grain volume increases, due to rising thermal stability factor. Although ATI is small for 2 Tbpsi and 9 grains/bit, as shown in Figs. 9 and 11, the writing sensitivity becomes worse, as shown in Fig. 13.

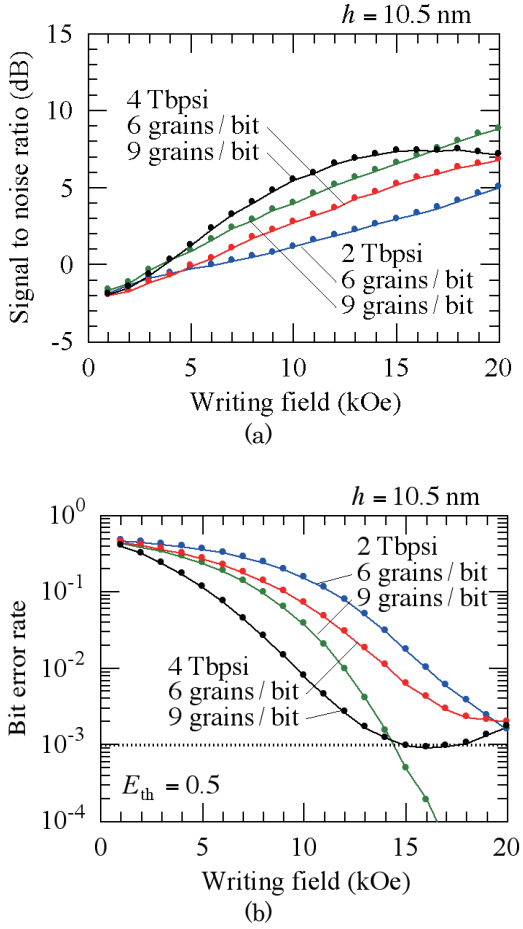

Fig. 13 Writing field dependence of (a) signal to noise ratio and (b) bit error rate under the condition of constant grain height h = 10.5 nm in 2 and 4 Tbpsi, and 6 and 9 grains/bit shingled HAMR.

In short, as far as we have examined, 9 grains/bit is suitable for 2 Tbpsi shingled HAMR where D_m = 5.0 nm, h = 4.4 nm, h/D_m = 0.89, and V = 110 nm^3, taking account of the results in Figs. 4, 8, 9, and 13. And 6 grains/bit is suitable for 4 Tbpsi where D_m = 4.2 nm, h = 10.5 nm, h/D_m = 2.5, and V = 184 nm^3, taking account of the results in Figs. 5, 8, 10, and 13.

The writing sensitivity for 4 Tbpsi is worse than that for 2 Tbpsi due to the smaller grain number per bit and the larger grain volume.

4. Conclusions

We examined ATI on shingled HAMR for all combinations of 2 and 4 Tbpsi, and 6 and 9 grains/bit.

As far as we have examined, 9 grains/bit is suitable for 2 Tbpsi shingled HAMR where the mean grain size D_m = 5.0 nm, the grain height h = 4.4 nm, the grain aspect ratio h/D_m = 0.89, and the grain volume V = 110 nm^3. And 6 grains/bit is suitable for 4 Tbpsi where D_m = 4.2 nm, h = 10.5 nm, h/D_m = 2.5, and V = 184 nm^3. First, the writing sensitivity for 4 Tbpsi shingled HAMR is worse than that for 2 Tbpsi due to the smaller grain number per bit. Second, since the grain temperature is higher for 4 Tbpsi due to the smaller grain pitch, the V value must be larger in order to improve ATI. As a result, the writing sensitivity is even worse, since the thermal stability factor increases as the V value increases. Therefore, 4 Tbpsi shingled HAMR has an intrinsic disadvantage over 2 Tbpsi shingled HAMR in terms of ATI.

Acknowledgement We acknowledge the support of the Advanced Storage Research Consortium (ASRC), Japan.

References

1) S. Kalarickal, A. Tsoukatos, S. Hernandez, C. Hardie, and E. Gage: *IEEE Trans. Magn.*, **55**, 3001804 (2019).
2) T. Kobayashi, Y. Nakatani, and Y. Fujiwara: *J. Magn. Soc. Jpn.*, **45**, 79 (2021).
3) M. Mansuripur and M. F. Ruane: *IEEE Trans. Magn.*, **MAG-22**, 33 (1986).
4) J. -U. Thiele, K. R. Coffey, M. F. Toney, J. A. Hedstrom, and A. J. Kellock: *J. Appl. Phys.*, **91**, 6595 (2002).
5) T. Kobayashi, Y. Isowaki, and Y. Fujiwara: *J. Magn. Soc. Jpn.*, **39**, 8 (2015).
6) T. Kobayashi, Y. Nakatani, and Y. Fujiwara: *J. Magn. Soc. Jpn.*, **44**, 34 (2020).
7) E. D. Boerner and H. N. Bertram: *IEEE Trans. Magn.*, **34**, 1678 (1998).
8) T. Kobayashi, Y. Nakatani, and Y. Fujiwara: *J. Magn. Soc. Jpn.*, **46**, 10 (2022).
9) T. Kobayashi, Y. Nakatani, and Y. Fujiwara: *J. Magn. Soc. Jpn.*, **42**, 127 (2018).
10) Y. Kanai, Y. Jinbo, T. Tsukamoto, S. J. Greaves, K. Yoshida, and H. Muraoka: *IEEE. Trans. Magn.*, **46**, 715 (2010).

Received Feb. 13, 2022; Accepted Mar. 12, 2022

J. Magn. Soc. Jpn., **46**, 58-63 (2022)

<Paper>

High Saturation Magnetization Calcium-Zinc Spinel Ferrite Prepared by Rapid Cooling

J. Hashimoto, K. Kakizaki, K. Kamishima

Graduate School of Science and Engineering, Saitama Univ., *255 Shimo-Okubo, Saitama 338-8570, Japan*

To obtain a high magnetization Ca-Zn-based spinel ferrite, we investigated the synthesis conditions and magnetic properties of samples with compositions of Ca: Zn: Fe = 0.5: 2.5: 16-x (x = 1, 2, 3, 4, 5, 6, and 7) sintered at 1300°C and then cooled under different conditions (-200°C/hour or quenched in water). Quenching the sample at x = 3 resulted in the best sample with the highest magnetization of 146 emu/g at T = 1.8 K. We estimated the Fe^{2+} amount and molar ratio of the sample by using thermogravimetry/ differential thermal analysis (TG/DTA). The large lattice constant implied that the spinel contained Ca^{2+} ions at its transition metal sites, which possibly led to a cationic distribution contributing to the high magnetization.

Key words: Ca-Zn-based spinel ferrite, high magnetization

1. Introduction

Ferrites are well-known ferrimagnets, which can be classified into two groups. The first is cubic spinel ferrites with chemical formulae of $MeFe_2O_4$, in which Me is a divalent cation like Mn, Co, and Zn.[1] The second is hexagonal ferrites, including a practically important magnet $BaFe_{12}O_{19}$ (M-type ferrite). M-type ferrite has S-blocks $(2Fe_3O_4)^{2+}$ and R-blocks $(BaFe_{12}O_{11})^{2-}$ alternately stacked up in the hexagonal c-axis. The structure of an S-block is identical to that of the cubic spinel ferrite. The intercalation of neutral S-blocks $(2MeFe_2O_4)^{0\pm}$ to M-type ferrite is possible to form another kind of hexagonal ferrite, W-type, with the chemical formula of $BaMe_2Fe_{16}O_{27}$. A kind of W-type hexagonal ferrite was reported to have a high coercivity of about 2 kOe and a saturation magnetization higher than that of M-type ferrite by about 10%.[2, 3]

On the other hand, calcium-doped M-type hexaferrite was reported with a high coercivity of H_C ~ 5 kOe.[4] This report motivated us to attempt to sinter samples having compositions of Ca: Sr: Zn: Fe = z: 1-z: 2: 16 at 1250°C for 5 hours in order to confirm the effect of adding CaO on the magnetic properties of Sr-based Zn_2W-type ferrite. At z = 1, we failed in synthesizing the W-type ferrite but obtained a mixed phase of spinel, $Ca_3Fe_{15}O_{25}$, and α-Fe_2O_3, which exhibited a high magnetization of about 50 emu/g at room temperature at 15 kOe.

To the best of our knowledge, Ca-based spinel ferrites have not been reported except for $Ca_xZn_{1-x}Fe_2O_4$ and $Ca_xFe_{3-x}O_4$.[5, 6] Non-substituted $CaFe_2O_4$ does not adopt a spinel structure but an orthorhombic structure with the space group of Pnma.[7] Moreover, the magnetizations of $Ca_3Fe_{15}O_{25}$ and α-Fe_2O_3 at room temperature at 15 kOe are relatively small; the former is about 15 emu/g, and the latter is about 0.5 emu/g.[8, 9]

The mixed-phase sample at z = 1 (Ca: Zn: Fe = 1: 2: 16) suggests the existence of high-magnetization spinel ferrites doped with Ca^{2+} and Zn^{2+}. To reduce the α-Fe_2O_3 phase, we attempted to produce samples having compositions of Ca: Zn: Fe = 1: 2: 16-x (x = 0, 1, 2, 3, 4, 5, 6, and 7) at 1300°C for 5 hours, and the cooling rate was -200°C/hour. Figures 1 and 2 show the X-ray diffraction patterns of these samples. Although the diffraction peaks of α-Fe_2O_3 were reduced by changing x, those of $Ca_3Fe_{15}O_{25}$ remained in all these samples. This preliminary experiment suggested the need to stabilize the spinel phase and prevent the formation of the $Ca_3Fe_{15}O_{25}$ phase, which led us to decrease the ratio of Ca/Zn.

The objective of this study is to synthesize the highest magnetization Ca-Zn-based spinel ferrite by changing the compositions.

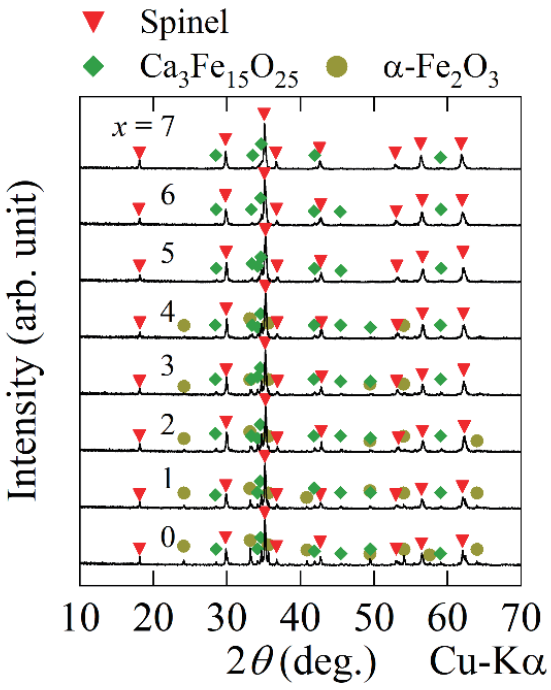

Fig. 1 XRD patterns of Ca: Zn: Fe = 1: 2: 16-x samples sintered at 1300°C and cooled at -200°C/hour in air.

Corresponding author: K. Kamishima
(e-mail: kamisima@mail.saitama-u.ac.jp)

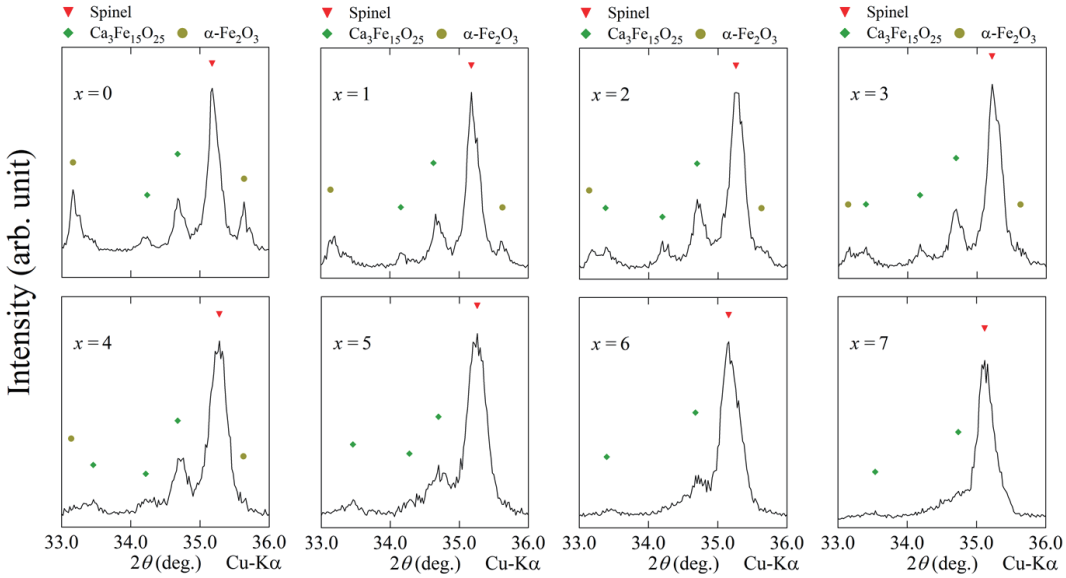

Fig. 2 XRD patterns of Ca: Zn: Fe = 1: 2: 16-x samples sintered at 1300°C and cooled at -200°C/hour in air (expanded).

2. Experimental Procedure

The calcium-zinc spinel ferrite samples were synthesized by solid state reaction. The starting materials of $CaCO_3$, ZnO, and α-Fe_2O_3 were mixed in a wet-ball-milling pot for 24 hours at Ca: Zn: Fe = 0.5 : 2.5 : 16-x. The mixed powders were dried and pressed into disks at 1 t/cm^2. The pressed samples were sintered at 1300°C for 5 hours. After being sintered, they were cooled at -200°C/hour in air or quenched in water.[5] Finally, they were ground into powders with a mortar.

The crystallographic phases of the samples were confirmed by using an X-ray diffractometer (Bruker, D8 Advance Eco). The magnetization was measured by using a vibrating sample magnetometer (Tamakawa, TM-VSM2130HGC) and a superconducting quantum interference device magnetometer (Quantum Design, MPMS 7). The elemental analysis of the samples was performed by energy-dispersive X-ray spectroscopy (EDX) with an X-ray detector (Bruker, Quantax 630M-129) in a scanning electron microscope (Hitachi High-Tech Science Corp., SU-1510) because the sublimation of ZnO possibly reduced the amount of zinc in the samples.[10] In order to estimate the amount of divalent iron in a sample, we used a thermogravimetric and differential thermal analyzer (Hitachi High-Tech Science Corp., TG:SII EXSTAR 6200 TMA).

3. Result & Discussion

Figures 3 and 4 show the X-ray diffraction patterns of the calcium-zinc spinel ferrite samples sintered at 1300°C and cooled in air. Although the secondary phases of $Ca_3Fe_{15}O_{25}$ and α-Fe_2O_3 were observed at $0 \leq x \leq 6$, the peak intensity of $Ca_3Fe_{15}O_{25}$ was drastically reduced compared to the case of Zn/Ca = 2 in Figs. 1 and 2. A decrease in the ratio of iron cations reduced the peak intensities of $Ca_3Fe_{15}O_{25}$ and α-Fe_2O_3 phases. It implies that the spinel structure became unstable due to excessive Fe^{3+} ions compared to Ca^{2+} ions.

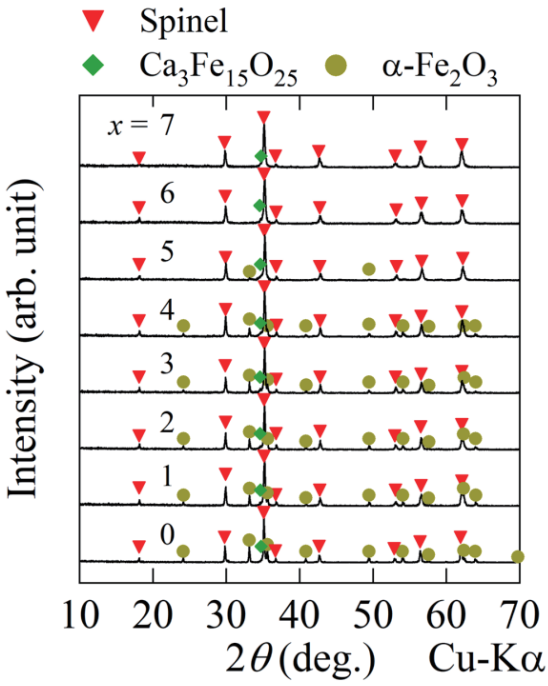

Fig. 3 XRD patterns of Ca: Zn: Fe = 0.5: 2.5: 16-x samples sintered at 1300°C and cooled at -200°C/hour in air.

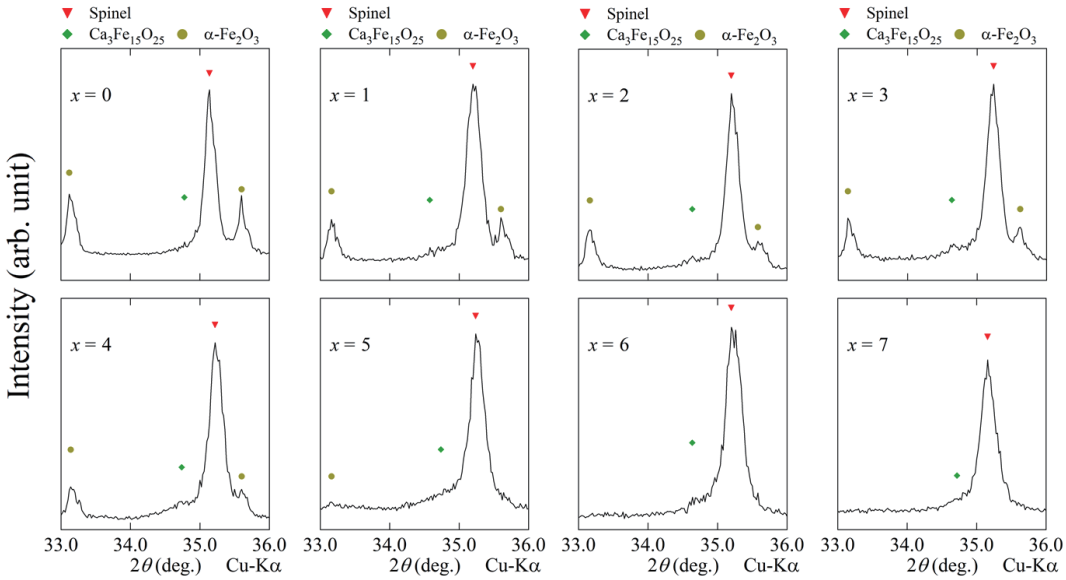

Fig. 4 XRD patterns of Ca: Zn: Fe = 0.5: 2.5: 16-x samples sintered at 1300°C and cooled at -200°C/hour in air (expanded).

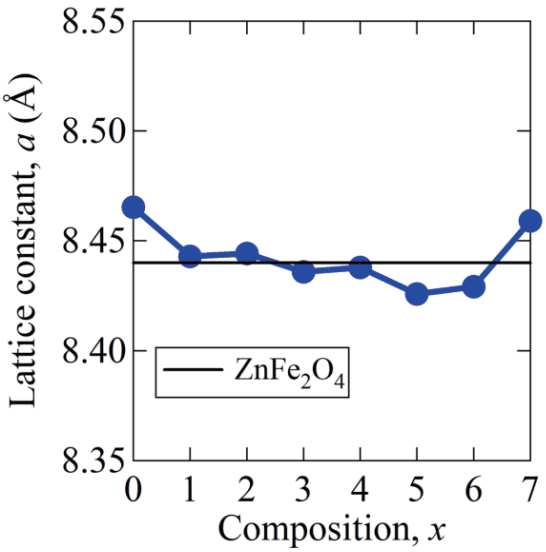

Fig. 5 Lattice constants of Ca: Zn: Fe = 0.5: 2.5: 16-x samples sintered at 1300°C and cooled at -200°C/hour in air.

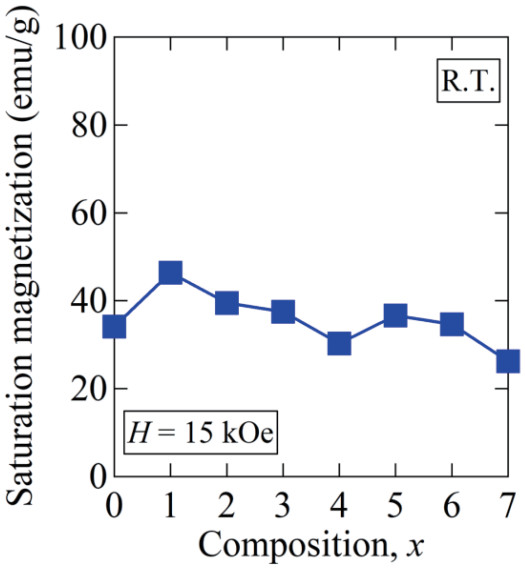

Fig. 6 Saturation magnetization of Ca: Zn: Fe = 0.5: 2.5: 16-x samples sintered at 1300°C and cooled at -200°C/hour in air.

Figure 5 shows the lattice constants of the spinel phase in these calcium-zinc spinel samples, where the solid line indicates the lattice constant of $ZnFe_2O_4$ (8.44 Å).[11] Although the lattice constants of some samples were larger than that of $ZnFe_2O_4$, the variation with increasing x was irregular. Therefore, this result suggests that Ca^{2+} ions were disorderly included in the spinel structure independent of x.

Figure 6 shows the saturation magnetization of these calcium-zinc spinel samples at room temperature. The maximum value was 46 emu/g at $x = 1$, where the sample contained the secondary phases of α-Fe_2O_3 and $Ca_3Fe_{15}O_{25}$. Although the sample at $x = 7$ exhibited almost the single spinel phase, it had the smallest magnetization. It indicates that the iron ratio of the spinel was reduced together with the decrease of α-Fe_2O_3. Therefore, it does not seem easy to obtain the high magnetization spinel just by changing the amount of Fe^{3+} ions. The formation of these secondary phases seemed to result from the decomposition of the samples associated with the relatively slow cooling process at -200°C/hour. In order to prevent this possible decomposition, we attempted to quench samples after sintering.

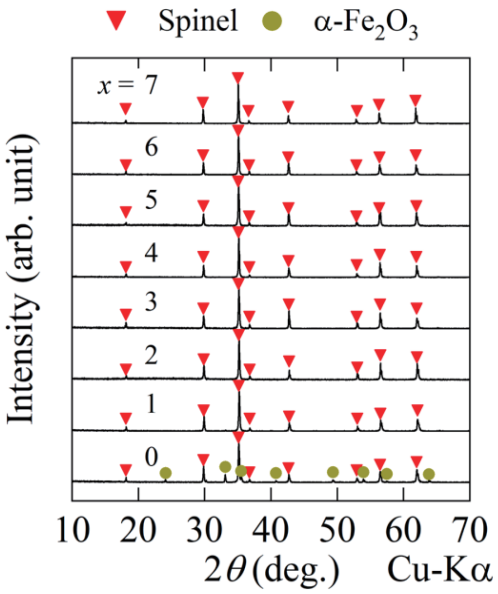

Fig. 7 XRD patterns of Ca: Zn: Fe = 0.5: 2.5: 16-x samples sintered at 1300°C and quenched in water.

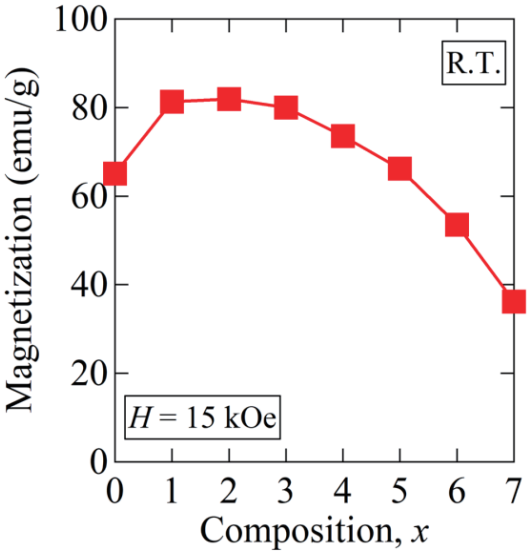

Fig. 9 Saturation magnetization of Ca: Zn: Fe = 0.5: 2.5: 16-x samples sintered at 1300°C and quenched in water.

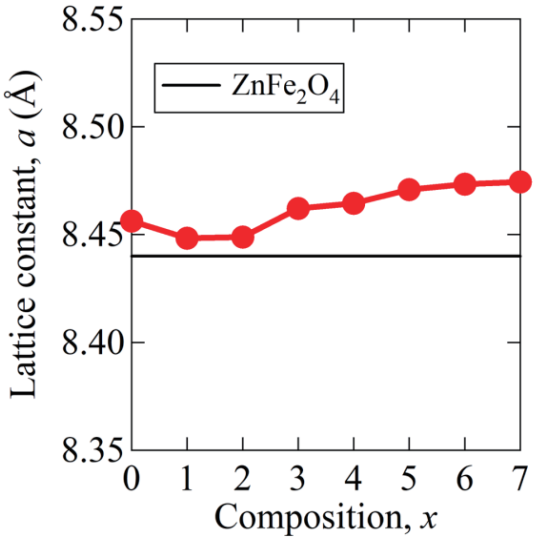

Fig. 8 Lattice constants of Ca: Zn: Fe = 0.5: 2.5: 16-x samples sintered at 1300°C and quenched in water.

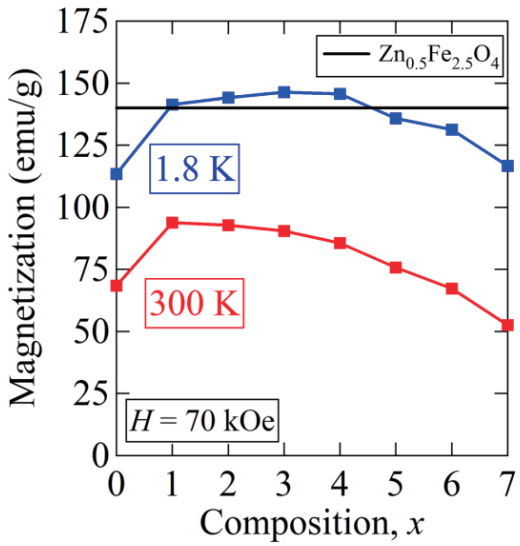

Fig. 10 Saturation magnetization of quenched samples measured at T = 300 K and 1.8 K.

Figure 7 shows the X-ray diffraction patterns of the calcium-zinc spinel ferrite samples sintered at 1300°C and quenched in water. The secondary phase of α-Fe_2O_3 was observed at $x = 0$, and the single phase of spinel was at $1 \leq x \leq 7$. These quenched samples did not exhibit the $Ca_3Fe_{15}O_{25}$ phase but consisted of the main spinel phase with high crystallinity in contrast with the samples cooled at -200°C/hour in air. The lattice constants of these quenched spinel samples were larger than that of $ZnFe_2O_4$, as shown in Fig. 8. This result implies that the spinel structure contained Ca^{2+} ions with an ionic radius of about 1 Å, larger than those of transition metal cations.[12)]

Figure 9 shows the saturation magnetization of the quenched samples at room temperature. The magnetization values were higher than those of the samples cooled at -200°C/hour in air as shown in Fig. 6.

These quenched samples had main spinel phases with larger lattice constants and higher magnetizations, which implies that the structure of the high magnetization calcium-zinc spinel is stable at high temperatures. In order to examine the intrinsic magnetization of these samples at low temperatures, we used a superconducting quantum interference device (SQUID) magnetometer.

Figure 10 shows the magnetization of the quenched samples measured at H = 70 kOe and T = 300 K and 1.8 K. The maximum value was 146 emu/g at x = 3, larger than that of Zn^{2+}-ion-doped magnetite (black line).[13)] The highest-magnetization sample consisted of the single spinel phase, as shown in Fig. 7.

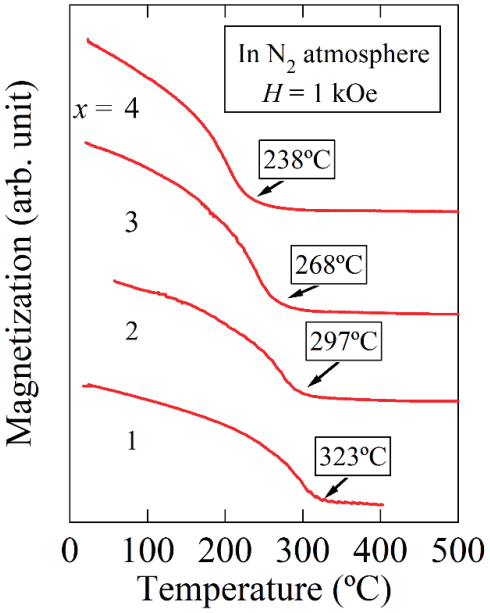

Fig. 11 Temperature dependence of magnetization of quenched samples with Ca: Zn: Fe = 0.5: 2.5: 16-x.

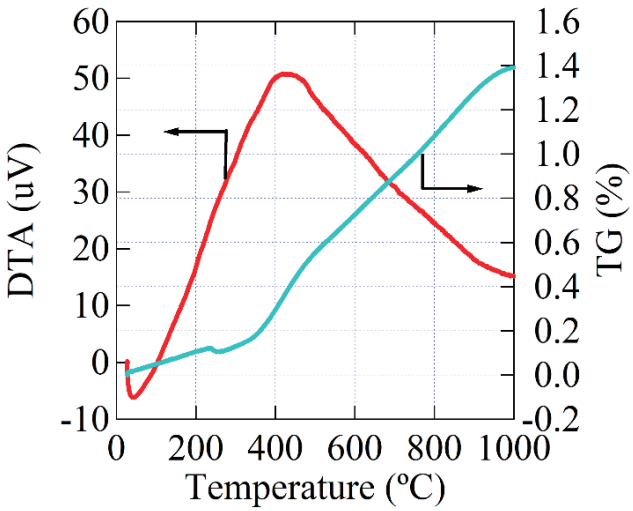

Fig. 12 TG-DTA of Ca: Zn: Fe = 0.5: 2.5: 13 sample sintered at 1300°C and quenched in water.

Figure 11 shows the temperature dependence of magnetization of the quenched samples with Ca: Zn: Fe = 0.5: 2.5: 16-x ($1 \leq x \leq 4$). There was only one T_C for each sample, demonstrating that these quenched samples consisted of the single phase of spinel crystallographically and magnetically. A decrease in the Fe^{3+} amount by $\Delta x = 1$ reduced the Curie temperature by ΔT_C of about 30°C.

The quenched samples had low electric resistivities of about ~ 10^{-2} Ω·cm, suggesting the existence of Fe^{2+} ions (as in magnetite Fe_3O_4 with a similar resistivity of 1×10^{-2} Ω·cm).[14] In order to estimate the Fe^{2+} amount, we attempted thermogravimetry/differential thermal analysis (TG-DTA) experiments.

Figure 12 shows the TG-DTA result of the sample at x = 3 (Ca: Zn: Fe = 0.5: 2.5: 13) sintered at 1300°C and quenched in water. The increase in mass was about 1.39 % of the starting weight of the sample. The energy dispersive X-ray spectroscopy (EDX) analysis of this sample showed that the composition of the sample was Ca: Zn: Fe = 0.5: 2.13: 13. Thus, assuming the increase came from the oxidization from Fe^{2+} to Fe^{3+}, we estimated the molar ratio in the sample as Ca^{2+}: Zn^{2+}: Fe^{2+}: Fe^{3+}: O^{2-} = 0.5: 2.13: 2.129: 10.871: 21.0655. The ratio can be normalized as the chemical composition of spinel ferrite. If Ca^{2+} ions are all located at transition metal sites, the ratio is Ca^{2+}: Zn^{2+}: Fe^{2+}: Fe^{3+}: O^{2-} = 0.095: 0.405: 0.404: 2.064: 4.

The magnetization of this sample was 146 emu/g at T = 1.8 K and H = 70 kOe. Thus, the Bohr magneton per this chemical formula unit was calculated to be 6.07 μ_B. Assuming that the spins at octahedral B sites are antiparallel to those at tetrahedral A sites in the spinel structure, the distribution of each ion can be estimated as follows,

$(Zn^{2+}_{0.405}Fe^{3+}_{0.587}\square_{0.008})_A$
$[Fe^{2+}_{0.404}Fe^{3+}_{1.477}Ca^{2+}_{0.095}\square_{0.024}]_B O^{2-}_4$
(□: vacant lattice).

On the other hand, if Ca^{2+} ions are all located at O^{2-} sites, the ratio is Ca^{2+}: Zn^{2+}: Fe^{2+}: Fe^{3+}: O^{2-} = 0.093: 0.395: 0.395: 2.016: 3.907. In this case, the distribution of each ion can also be estimated as follows,

$(Zn^{2+}_{0.395}Fe^{3+}_{0.573}\square_{0.032})_A$
$[Fe^{2+}_{0.395}Fe^{3+}_{1.443}\square_{0.162}]_B Ca^{2+}_{0.093}O^{2-}_{3.907}$
(□: vacant lattice).

Here, Fe^{2+} ions in the quenched sample are considered to occupy B sites, as in magnetite, because the low electric resistivity of the sample implies the hopping conduction caused by mixed-valence iron cations at B sites. It is also empirically known for Zn^{2+} to occupy tetrahedral A sites.[11] Then, the possible distributions of Ca cations need considered. The ionic radius of Ca^{2+} (1 Å) is much larger than those of transition metal ions (Zn^{2+}, Fe^{2+}, Fe^{3+} : 0.6 ~ 0.78 Å) and it seems to be too large to occupy tetrahedral A sites for Ca^{2+} ion. Actually, the coordination number of a calcium cation is reported to be above six. [12] Thus, both of the above estimations reflect the strong tendency for Zn^{2+} ions to occupy tetrahedral A sites, and the two possible extreme cases are considered for Ca^{2+} ions to occupy either transition metal sites or oxygen sites. However, if all Ca^{2+} ions were located at O^{2-} sites (the latter case), its lattice constant might be smaller than the lattice constants in Fig. 6 due to the smaller ionic radius of Ca^{2+} ion than that of O^{2-}. On the other hand, it is also unlikely that all the Ca^{2+} ions occupy octahedral B sites because of the significant difference in the ionic radii between Ca^{2+} (1 Å), Fe^{2+} (0.780 Å), and Fe^{3+} (0.645 Å).[12] Therefore, even a small

substitution of Ca^{2+} for transition metal cations at B sites is expected to expand the lattice constant. Thus, the quenched spinel possibly took the distribution between the two cases mentioned above.

4. Conclusion

Our attempts to synthesize Ca-Zn-based W-type ferrites led us to discover a high magnetization spinel phase as a by-product possibly not corresponding to the stoichiometry of spinel. We found the synthesis condition of the spinel with the composition at Ca: Zn: Fe = 0.5: 2.5: 16-x by sintering at 1300°C and quenching in water. The best sample was obtained with composition of Ca: Zn: Fe = 0.5: 2.5: 13 (x = 3), and the saturation magnetization was 146 emu/g at T = 1.8 K. Although the expansion of the lattice constant implied that the spinel contained Ca^{2+} cations at its transition-metal sites, the distribution was not completely determined.

Further work needs to be done to determine the exact cation distribution to understand the high intrinsic magnetization.

References

1) S. Blundell: Magnetism in Condensed Matter, p. 97 (Oxford Univ. Press, 2001).
2) F. K. Lotgering, P. H. G. M. Vromans, and M. A. H. Huyberts: *J. Appl. Phys.*, **51**, 5913 (1980).
3) G. Albanese, M. Carbucicchio, and G. Asti: *Appl. Phys.*, **11**, 81 (1976).
4) Y. Kobayashi, S. Hosokawa, E. Oda, and S. Toyota: *J. Jpn. Soc. Powder Powder Metallurgy*, **55**, 541 (2008).
5) E. W. Gorter: *Philips Res. Rep.*, **9**, 356 (1954).
6) J. De Sitter, A. Govaert, E. De Grave, D. Chambaere, and G. Robbrecht: *Phys. Stat. sol. (a)*, **43**, 619 (1977).
7) B. F. Decker and J. S. Kasper: *Acta Cryst.*, **10**, 332 (1957).
8) R. Gerardin, E. Millon, A. Bonazebi, J. F. Brice, F. Jeannot, and O. Evrard: *J. Phys. Chem. Solids*, **49**, 343, (1988).
9) S. T. Lin: *Phys. Rev.*, **116**, 1447 (1959).
10) D. F. Anthrop and A. W. Searcy: *J. Phys. Chem.*, **68**, 2335 (1964).
11) J. Smit and H. P. J. Wijn: Ferrites, p. 136 (Philips Technical Library, Netherlands 1959).
12) R. D. Shannon: *Acta Cryst. A*, **32**, 751 (1976).
13) J. J. Went and E. W. Gorter: *Philips Tech. Rev.*, **13**, 181 (1952).
14) S. Borroni, E. Baldini, V. M. Katsukuri, A. Mann, K. Parlinski, D. Legut, C. Arrell, F. van Mourik, J. Teyssier, A. Kozlowski, P. Piekarz, O. V. Yazyev, A. M. Oleś, J. Lorenzana, and F. Carbone: *Phys. Rev. B*, **96**, 104308 (2017).

Received Jan. 6, 2022; Accepted Feb. 23, 2022.

J. Magn. Soc. Jpn., **46**, 64-69 (2022)

<Paper>

Development of $BiFeO_3$-based multiferroic thin films with large saturation magnetization and perpendicular magnetic anisotropy - The effect of the Co substitution against Fe on magnetic properties -

T. Ozeki[1], D. Yamamoto[1], G. Egawa[2], and S. Yoshimura[2]

[1] Department of Materials Science, Graduate School of Engineering Science, Akita University

1-1 TegataGakuen-machi Akita, Akita 010-8502, Japan

[2] Research Center of Advanced Materials for Breakthrough Technology, Graduate School of Engineering Science, Akita University

1-1 TegataGakuen-machi Akita, Akita 010-8502, Japan

High saturation magnetization and perpendicular magnetic anisotropy are required for ferromagnetic / ferroelectric thin films to apply magnetic recording such as magnetic writing elements of magnetic wire memory, which is a next-generation device with very high recording density. To realize the magnetic properties, substitution of Co against Fe in $(Bi_{1-x}Ba_x)FeO_3$ and $(Bi_{1-x}La_x)FeO_3$ thin films were investigated. In the $(Bi,Ba)(Fe,Co)O_3$ thin films, both Ba and Co substitution up to several tens at% had contribution to increase the saturation magnetization. The high saturation magnetization was obtained in $(Bi,Ba)(Fe,Co)O_3$ thin films with the total composition of Ba and Co of around 60 at%. Further increment of Ba and Co substitution decreased the saturation magnetization because the formation of the $BiFeO_3$ phase is hindered by an excess amount of Ba and Co with larger ion radius than Bi and Fe. Co substitution up to 20 at% had contribution to increase the perpendicular magnetic anisotropy. In the $(Bi,La)(Fe,Co)O_3$ thin films, the effect of La substitution was not large to increase the saturation magnetization and perpendicular magnetic anisotropy, however the effect of Co substitution up to 30 at% was large to increase the saturation magnetization and perpendicular magnetic anisotropy.

Keywords: Multiferroic thin films, Element substitution, Saturation magnetization, Perpendicular magnetic anisotropy, New magnetic recording devices

1. Introduction

Increasing the recording density of hard disk drives (HDDs) has contributed to the development of information society for a long time. Recently, energy-assisted magnetic recording technologies for HDDs, such as thermally-assisted magnetic recording[1)] and microwave-assisted magnetic recording[2)] have been widely studied in order to decrease the switching field for magnetic writing. However, these days, the increment ratio of the recording density in HDDs is becoming gradually slow. In this regard, the newly proposed magnetic memory with magnetic nanowires is a hopeful device with a very large capacity. However, magnetic writing in this memory is problematic. Suppose this memory will use a magnetic writing head of HDDs for the magnetic writing. In that case, the power consumption for the magnetic writing will become huge because this memory will need many magnetic writing heads with the same number of magnetic nanowires.

In recent years, magnetization reversal by an electric field has attracted attention as a method for reducing the power consumption of writing, for which various materials and methods have been studied[3)-10)]. One of the fascinating materials for this process is multiferroic (ferromagnetic/ferroelectric) materials, which can control the magnetization direction only by applying an electric field. $BiFeO_3$ (BFO), which has antiferromagnetism and ferroelectricity at room temperature, is well-known as a typical multiferroic material[11)]. It has been reported that ferromagnetism and ferroelectricity can be obtained in $(Bi_{1-x}Ba_x)FeO_3$ (BBFO) in which a part of Bi of BFO is substituted by Ba[12)]. In addition to this result, it has been reported that in the thin films, a part of Bi (A-site) or Fe (B-site) was substituted by La or Co in order to introduce the ferromagnetism in BFO[13)-17)]. For the past few years, we have fabricated high-quality $BiFeO_3$-based ferromagnetic/ferroelectric thin films by using pulsed DC reactive sputtering method[18)], which is effective for deposition of oxide and nitride thin films of suppression of arc discharged during sputtering. As a result, saturation magnetization (M_s) of about 90 emu/cm^3 was obtained in the BBFO thin film[19)], 1.5 times higher than that of BBFO thin films prepared by radio-frequency (RF) (13.56 MHz) sputtering method[20)]. The reason for this improvement was the acceleration of the $BiFeO_3$ phase crystallization. In addition, although the M_s of the $(Bi,La)(Fe,Co)O_3$ (BLFCO) thin film fabricated by the pulsed DC reactive sputtering method was not so high (i.e., 70 emu/cm^3), it had a large coercivity of about 4.0 kOe with the direction to the perpendicular film plane and perpendicular magnetic anisotropy[21,22)].

Here, a new writing method, "Magnetization transfer by an electric field," is proposed for magnetic memory with magnetic nanowires. Consider the laminated film with magnetic interactions between the ferromagnetic thin film (magnetic nanowire) and the

Corresponding author: S. Yoshimura
(e-mail: syoshi@gipc.akita-u.ac.jp).

multiferroic (ferromagnetic/ferroelectric) thin film; in which, the magnetization reversal of the metallic ferromagnetic thin film (magnetic nanowire) via magnetization reversal of the multiferroic (ferromagnetic/ferroelectric) thin film is performed by applying an electric field to the laminated film. This method will be useful for magnetization reversal by an electric field in magnetic memory with magnetic nanowires, because of the simple structure of writing elements and the reduced power consumption of writing process.

To realize the "Magnetization transfer by an electric field," in the laminated film with the ferromagnetic thin film and the multiferroic thin film, a multiferroic thin film with high M_s and perpendicular magnetic anisotropy are needed. So, we have to induce the perpendicular magnetic anisotropy in BBFO thin films or increase the M_s in BLFCO thin films. Here large M_s and perpendicular magnetic anisotropy were not observed in $(Bi,La)FeO_3$ thin films. This indicates that the Co substitution against Fe seems to induce the perpendicular magnetic anisotropy and increase the M_s.

In this study, we focused on the Co substitution amount against Fe in $(Bi,Ba)(Fe,Co)O_3$ (BBFCO) thin films and BLFCO thin films, and we investigated the effect of the Co substitution amount against Fe on the magnetic properties including M_s and perpendicular magnetic anisotropy.

2. Experimental Procedure

Multilayers of Ta (5 nm)/ Pt (100 nm)/ $(Bi_{1-x}M_x)(Fe_{1-y}Co_y)O_3$ (M: Ba, La) (200 nm) were deposited onto a thermally oxidized Si wafer using a ultrahigh-vacuum (UHV) sputtering system. The Ba concentration x was varied from 0.22 to 0.78. The Co concentration y was varied from 0 to 0.36. The Ta seedlayer, Pt underlayer, and $(Bi_{1-x}M_x)(Fe_{1-y}Co_y)O_3$ layer were deposited at room temperature, 400 °C, and 695 °C, respectively. The film thickness and deposition temperature of the Ta seedlayer and Pt underlayer were optimized to obtain a strong (111) orientation of the Pt underlayer[23]. The very high frequency (VHF) (40.68 MHz) plasma irradiation[24] during the reactive pulsed DC sputtering deposition of $(Bi_{1-x}M_x)(Fe_{1-y}Co_y)O_3$ thin films were performed with an electric power of 5 W to obtain the crystal grain growth of the $BiFeO_3$ phase. The frequency of the DC pulse was fixed at 100 kHz. Here, the duty ratios between sputtering ON and OFF were 3 and 2, for example, the time of sputtering ON was 6 μs, and that of OFF was 4 μs for 100 kHz. The sputtering power of the pulsed DC was fixed at 150 W. The compositions of the fabricated $(Bi_{1-x}M_x)(Fe_{1-y}Co_y)O_3$ thin films were analyzed by energy-dispersive X-ray spectroscopy (EDS). The crystallographic orientations and crystalline structures of the fabricated $(Bi_{1-x}M_x)(Fe_{1-y}Co_y)O_3$ thin films were analyzed by X-ray diffraction (XRD) analysis. The magnetization curves of $(Bi_{1-x}M_x)(Fe_{1-y}Co_y)O_3$ thin films were measured using a vibrating sample magnetometer (VSM) with the application of an in-plane/out-of-plane magnetic field to the film surface. The demagnetizing field perpendicular to the film plane was canceled in the out-of-plane magnetization curves.

3. Results and Discussions

3.1 $(Bi,Ba)(Fe,Co)O_3$ thin film

Figure 1(a) shows the dependence of the M_s on the Ba concentration in A-site for the BBFCO thin films with the Co concentration on B-site as 0, 20, and 36 at% (BBFC0O, BBFC20O, and BBFC36O). With increasing the Ba concentration, M_s increased, attributed to the transformation from the antiferromagnetic phase to the ferrimagnetic phase[12]. The mechanism explains that a part of Fe^{3+} with a large magnetic moment is converted to Fe^{4+} with a small magnetic moment by substituting a part of Bi^{3+} with Ba^{2+} to maintain the balance of valences in the lattice. After the M_s showed maximum value at a certain value of the Ba concentration, the M_s decreased. This is due to the inhibition of the formation of the $BiFeO_3$ phase[19], because the diameter of ion Ba^{2+} is 1.21 times larger than that of Bi^{3+}. The Ba concentration, which showed the maximum M_s value, was not the same among every BBFCO thin film with different Co concentrations. With increasing the Co concentration from 0 to 36 at%, the Ba concentration which showed the maximum M_s value, decreased from 55 to 36 at%. From these data, the suitable amount of Ba and Co substitution for obtaining high M_s is found to be around 60 at%.

Figure 1(b) shows the dependence of the M_s on the Co concentration in the BBFCO thin films with a certain value of Ba concentration which showed the maximum M_s value for each BBFCO thin film. With increasing Co concentration up to 20 at%, M_s increased. This indicates that the Co substitution of Fe (B-site) up to 20 at% in BBFCO thin films was effective to increase the M_s. The decrease in M_s in the BBFCO thin films with the Co concentration of more than 20 at% was due to the inhibition of the formation of the $BiFeO_3$ phase. The reason of these changes will be discussed later in this section.

Figure 2(a) shows the dependence of the in-plane $H_{c//}$ and out-of-plane $H_{c\perp}$ on the Co concentration in the BBFCO thin films with a certain value of Ba

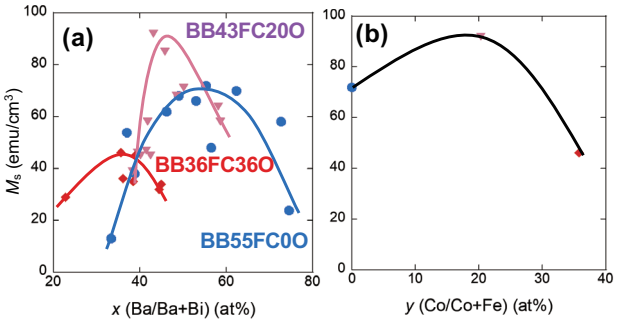

Fig. 1 Dependence of saturation magnetization on the (a) Ba and (b) Co concentration in BBFCO films.

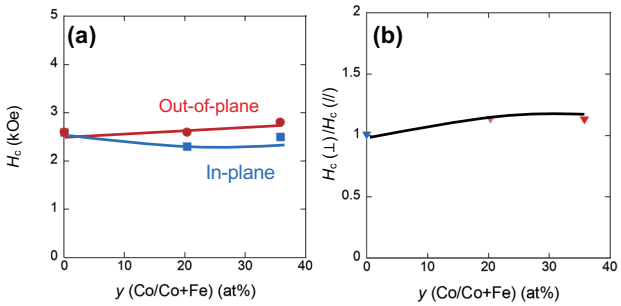

Fig. 2 Dependence of (a) H_c and (b) $H_{c\perp}/H_{c//}$ on Co concentration in BBFCO films.

concentration which showed the maximum M_s value for each BBFCO thin film. Figure 2(b) shows the dependence of the ratio between $H_{c//}$ and $H_{c\perp}$, indicating the perpendicular magnetic anisotropy, on the Co concentration in the BBFCO thin films. With increasing the Co concentration up to 20 at%, $H_{c//}$ decreased and $H_{c\perp}$ increased slightly. Therefore, $H_{c\perp}/H_{c//}$ also increased slightly. By further increasing the Co concentration to more than 20 at%, $H_{c//}$, $H_{c\perp}$, and $H_{c\perp}/H_{c//}$ were constant. From these results, it can be stated that the Co substitution of Fe (B-site) up to 20 at% will have been effective in increasing the perpendicular magnetic anisotropy in BBFCO thin films. However, the effect of the Co substitution on the perpendicular magnetic anisotropy was smaller than that on the saturation magnetization.

Figure 3 shows the in-plane and out-of-plane magnetization (*M-H*) curves measured by VSM with the magnetic field of parallel and perpendicular to film plane in BBFCO thin films with Ba and Co concentration of 55 and 0 at% (BB55FC0O), 43 and 20 at% (BB43FC20O), and 36 and 36 at% (BB36FC36O), respectively. These films showed the maximum M_s value for BBFCO samples with each Co concentration. The clear ferromagnetic (*M-H*) curves are shown. Here, a clear ferroelectric (*P-E*) curve measured by a ferroelectric tester with the electric field perpendicular to the film plane of the BBFC0O thin film was also shown in the previous work[19]. These indicate that this film had a multiferroic property with ferromagnetism and ferroelectricity.

Figure 4 shows the dependence of the (a) H_c and (b) squareness (S=M_r(remnant magnetization)/M_s) on the VSM measuring angle between magnetic field and film plane of BBFCO samples which are shown in Figure 3. The H_c and S measured with 0 degree indicates the in-plane H_c and S, and those with 90 degrees indicate the

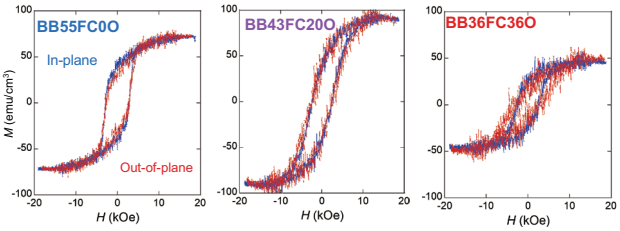

Fig. 3 In-plane and out-of-plane magnetization curves of BBFCO films with various Co concentration.

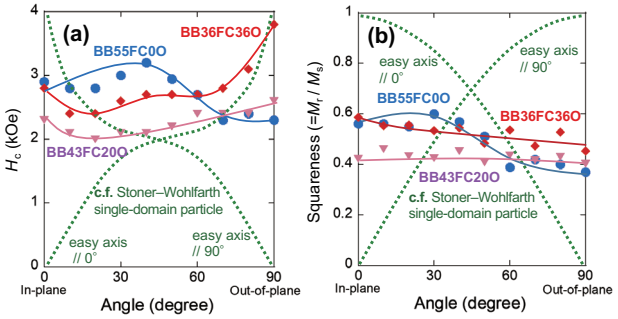

Fig. 4 Dependence of coercivity (a) and squareness (b) on the VSM measuring angle between magnetic field in BBFCO films.

out-of-plane H_c and S. To recognize the magnetic anisotropy of these films, the dependence of the H_c and S of Stoner-Wohlfarth single-domain particle on the angle between the magnetic field and easy or hard axis are also shown in these figures. With increasing the angle, the H_c and S decreased, and the lowest H_c and S were obtained at 90 degrees for BB55FC0O thin film. This tendency is a little similar to the case of Stoner-Wohlfarth single-domain particle with the easy axis of 0 degree. For BB43FC20O and BB36FC36O thin films, with increasing the angle, the S also decreased. However, the H_c increased with increasing the angle, and the highest H_c were obtained at 90 degrees for these films. This tendency is a little similar to the case of Stoner-Wohlfarth single-domain particle with an easy axis of 90 degrees. This indicates that BB43FC20O and BB36FC36O thin films had somewhat perpendicular magnetic anisotropy. The reason for the increase of perpendicular magnetic anisotropy by Co substitution should be discussed in a future study by using e.g., synchrotron radiation. However, we can say these magnetic properties of BB43FC20O thin film cause it to be a suitable candidate for novel magnetic devices.

The reason for the increase of saturation magnetization by Ba substitution in A-site and the decrease of saturation magnetization by excessive Ba substitution are as described in Figure 1 (a). Here, the

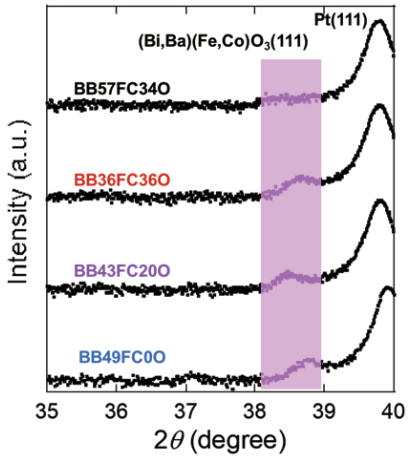

Fig. 5 XRD profiles of BBFCO films on Ta/Pt layer with various Co concentration.

factors of the increase of saturation magnetization by Co substitution up to 20 at% and the decrease of saturation magnetization by excessive Co substitution of more than 20 at% will be considered from the XRD analysis. Figure 5 shows the XRD profiles of BBFCO thin films with various Ba and Co substitutions. In the case of the BBFO thin film, by substituting with Ba, which has an ionic radius 1.22 times larger than that of Bi, the BBFO lattice became 0.5 % larger with Ba substitution of 10 at%[19]. Based on this, from the diffraction peak positions of BB49FC0O, BB43FC20O, and BB36FC36O, it was found that the BBFCO lattice became 0.25 % larger with Co substitution of 20 at%, and as a result, it was estimated that the ion radius of Co was 1.06 times larger than that of Fe^{3+}. This value is almost the same as the low-spin Co^{2+} ion radius (1.08 times larger than that of Fe^{3+}). Therefore, the increasing factor of saturation magnetization by Co substitution in B-site may be the transformation from the antiferromagnetic phase to the ferrimagnetic phase, which had Fe^{3+} with a large magnetic moment and Co^{2+} with a small magnetic moment. In the case of $Bi(Fe,Co)O_3$, it is known that weak ferromagnetism is exhibited instead of ferrimagnetism by the Co substitution with Fe[14),17)], but the thin film of this material had a polarization direction and a magnetization direction perpendicular to each other (in-plane magnetization). This is different from this BBFCO thin film, which tended to have a polarization direction and a magnetization direction parallel to each other (perpendicular magnetization). Therefore, it is considered that the mechanism to increase the saturation magnetization by the Co substitution is different depending on the presence or absence of elemental substitution at the A-site. Here, in order to obtain a large saturation magnetization in BBFCO of ferrimagnetic material, it is considered that the number of Fe^{3+} with a large magnetic moment and the sum of Fe^{4+} and Co^{2+} with a small magnetic moment should be roughly equal. This agrees that a suitable amount of Ba and Co substitution to obtain high M_s is nearly around 60 at% as mentioned in Figure 1(a). Here, to form ideal Ferrimagnetism, Fe^{3+} and (Co^{2+} or Fe^{4+}) should be arranged alternately. However, in BBFCO thin film, these arrangements were not controlled, and there were four combinations of adjacent B-site ions: Fe^{3+} and Co^{2+}, Fe^{3+} and Fe^{4+}, Fe^{4+} and Co^{2+} Fe^{3+} and Fe^{3+}, and they are considered to be randomly arranged. Therefore, the saturation magnetization of BBFCO thin film seems to be about half of the ideal (maximum expected) saturation magnetization. We believe that, in the future, a further increase in saturation magnetization can be realized by controlling the arrangement of ions to arrange ideal magnetic moments. The reason for the decrease in the saturation magnetization when the Co substitution amount exceeds 20 at% in BBFCO is the large strains in the lattice of the BBFCO thin film and the inhibition of the formation of the $BiFeO_3$ phase, because of the large amount of substitution with large ion radius of Ba^{2+} and

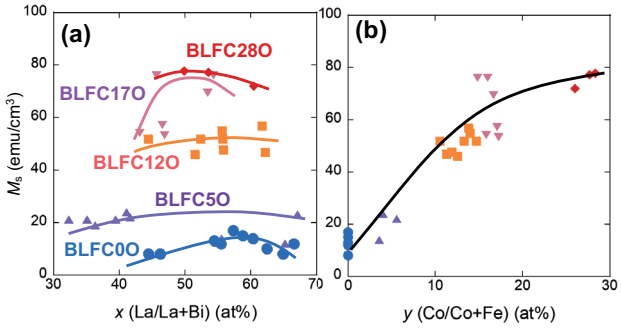

Fig. 6 Dependence of saturation magnetization on the (a) La and (b) Co concentration in BLFCO films.

Co^{2+}. An example of this is shown in the XRD profile of the BB57FC34O thin film.

3.2 $(Bi,La)(Fe,Co)O_3$ thin film

Figure 6(a) shows the dependence of the M_s on the La concentration in A-site for the BLFCO thin films with Co concentration on B-site as 0, 5, 12, 17, and 28 at% (BLFC0,BLFC5O, BLFC12O, BLFC17O, and BLFC28O). With increasing the La concentration up to around 50 at%, M_s increased a little. With further increasing the La concentration, the M_s decreased a little. This tendency is different from the case of BBFCO thin films. The reason for this difference will be discussed later in this section. Here, the La concentration dependence of M_s seems smaller than that of the Co concentration.

Figure 6(b) shows the dependence of the M_s on the Co concentration in the BLFCO thin films with the La concentration of around 50 at%. With increasing the Co concentration, M_s increased. This indicates that the Co substitution of Fe (B-site) in BLFCO thin films was very effective in increasing the M_s compared with the case of BBFCO thin films, especially the case of Co concentration of more than 20 at%. The reason for this difference will also be discussed later in this section.

Figure 7(a) shows the dependence of the in-plane $H_{c//}$ and out-of-plane $H_{c\perp}$ on the Co concentration in the BLFCO thin films with the La concentration of around 50 at%. Figure 7(b) shows the dependence of the ratio between $H_{c//}$ and $H_{c\perp}$, which indicates the perpendicular magnetic anisotropy on the Co concentration in the BLFCO thin films. By the Co substitution, $H_{c//}$ decreased drastically, and with the Co substitution of more than 10%, $H_{c//}$ became a constant value of about 2 kOe. On the

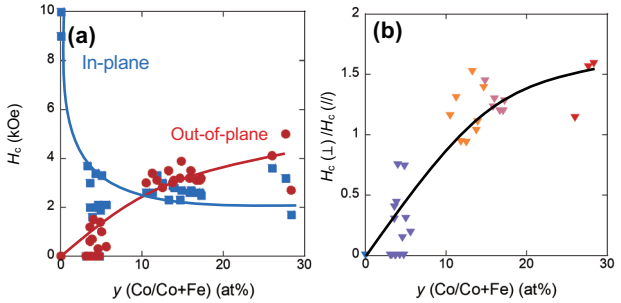

Fig. 7 Dependence of (a) H_c and (b) $H_{c\perp}/H_{c//}$ on the Co concentration in BLFCO films.

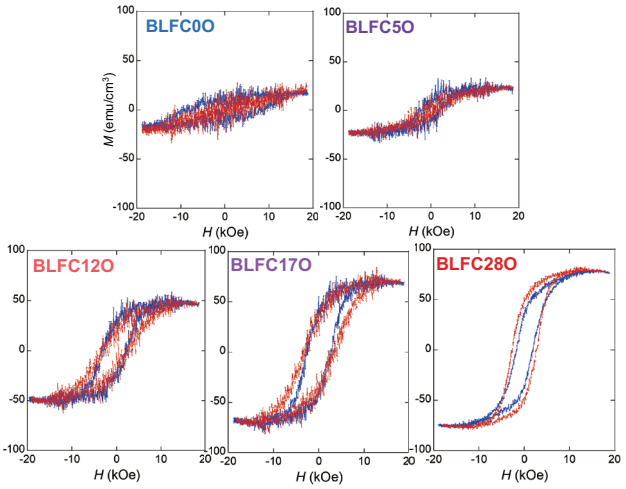

Fig. 8 In-plane and out-of-plane magnetization curves of BLFCO films with various Co concentration.

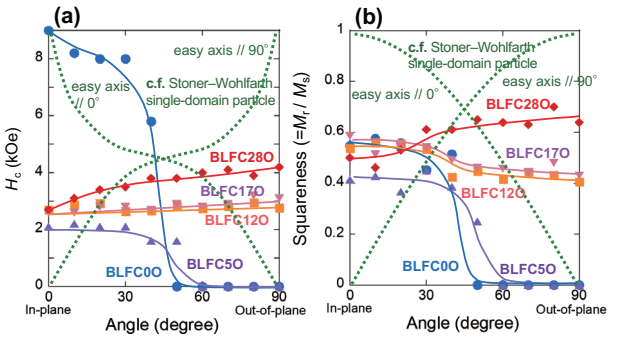

Fig. 9 Dependence of coercivity (a) and squareness (b) on the VSM measuring angle between magnetic field in BLFCO films.

other hand, $H_{c\perp}$ clearly and gradually increased up to 4 kOe with increasing the Co concentration. Therefore, $H_{c\perp}/H_{c//}$ also increased clearly with increasing the Co concentration. From these results, it can be inferred that the Co substitution of Fe (B-site) will have considerable effect in increasing the perpendicular magnetic anisotropy in BLFCO thin film.

Figure 8 shows the in-plane and out-of-plane magnetization (*M-H*) curves measured by VSM with the magnetic field of parallel and perpendicular to film plane in BLFCO thin films with the La concentration of around 50 at% and the Co concentration of 0, 5, 12, 17, and 28 at%, respectively. These films showed the maximum M_s value for BLFCO samples with each Co concentration. The clear ferromagnetic (*M-H*) curves are also shown. The ferroelectric (*P-E*) curve measured by a ferroelectric tester with the electric field of perpendicular to film plane of the BLFC28O thin film was also shown in previous work[22]. This indicates that this film had a multiferroic property with ferromagnetism and ferroelectricity.

Figure 9 shows the dependence of the (a) H_c and (b) S on the VSM measuring angle between magnetic field and film plane of BLFCO samples which are shown in Figure 8. The H_c and S decreased with increasing the angle, and the lowest H_c and S were obtained at 90 degrees for BLFC0O and BLFC5O thin films. This tendency is similar to the case of Stoner-Wohlfarth single-domain particle with the easy axis of 0 degree. For BLFC12O and BLFC17O thin films, with increasing the angle, the S also decreased. However, the H_c increased with increasing the angle, and the highest H_c were obtained at 90 degrees for these films. This indicates that BLFC12O and BLFC17O thin films had somewhat perpendicular magnetic anisotropy. With increasing the angle, the H_c and S increased, and the highest H_c and S were obtained at 90 degrees for BLFC28O thin film. This tendency is similar to the case of Stoner-Wohlfarth single-domain particle with an easy axis of 90 degrees. This indicates that BLFC28O thin film had clear perpendicular magnetic anisotropy. The reason for the increase of perpendicular magnetic anisotropy by the Co substitution should be discussed in a future study by using e.g., synchrotron radiation, but we can say these magnetic properties of BLFC28O thin film cause it to be a suitable candidate for novel magnetic devices.

Different tendencies of change of the saturation magnetization between La substitution in A-site and Co substitution in B-site will be considered. The further increase of saturation magnetization by excessive Co substitution of more than 20 at% will be considered. The mechanism of the saturation magnetization independence by La substitution may be that the large magnetic moment Fe^{3+} did not change to a small magnetic moment of Fe^{4+} because the valence balance in the lattice did not change even if a part of Bi^{3+} was substituted by La^{3+}. This is not the same situation as BBFCO thin films. On the other hand, the increasing mechanism of the saturation magnetization by Co substitution may be the transformation from the antiferromagnetic phase to the ferrimagnetic phase, which had Fe^{3+} with a large magnetic moment and Co^{2+} with a small magnetic moment. This is the same situation as BBFCO thin films. The reason for the further increase in the saturation magnetization when the Co substitution amount exceeded 20 at% in BLFCO in films is the small strains in the lattice of the BLFCO thin film and the formation of the $BiFeO_3$ phase. This is due to the small difference of ion radius between La^{3+} and Bi^{3+} (La^{3+} is 0.99 times against Bi^{3+}). This is not the same situation as BBFCO thin films.

4. Conclusion

In this study, we fabricated $(Bi_{1-x}M_x)(Fe_{1-y}Co_y)O_3$ (M: Ba, La, x: 0.22 - 0.78, y: 0 - 0.36) multiferroic thin films deposited by pulsed DC reactive sputtering method using a UHV sputtering system. We investigated the effect of the Co substitution amount against Fe in (Bi,Ba)(Fe,Co)O_3 thin films and (Bi,La)(Fe,Co)O_3 thin films on the magnetic properties such as saturation magnetization and perpendicular magnetic anisotropy. With increasing the Co concentration up to 20 at%, saturation magnetization and perpendicular magnetic

anisotropy increased in $(Bi,Ba)(Fe,Co)O_3$ and $(Bi,La)(Fe,Co)O_3$ thin films. Especially in the case of $(Bi,La)(Fe,Co)O_3$ thin films, the Co concentration of more than 20 at% was also effective. The reason for the increase of saturation magnetization on Co substitution is the transformation from the antiferromagnetic phase to the ferrimagnetic phase, which had Fe^{3+} with a large magnetic moment and Co^{2+} with a small magnetic moment. Furthermore, the reason for the further increase of saturation magnetization on Co substitution of more than 20 at% in $(Bi,La)(Fe,Co)O_3$ thin films is the small strains in the lattice of the $(Bi,La)(Fe,Co)O_3$ thin film and the formation of the $BiFeO_3$ phase. These magnetic properties with high saturation magnetization and perpendicular magnetic anisotropy are suitable for novel magnetic devices.

References

1) J. U. Thiele, S. Maat, and E. E. Fullerton: *Appl. Phys. Lett.*, **82**, 2859 (2003).
2) J. G. Zhu, X. Zhu, and Y. Tang: *IEEE Trans. Magn.*, **44**, 125 (2008).
3) J. Ryu, A. V. Carazo, K. Uchino, and H.-E. Kim: *Japanese J. Appl. Phys.*, **40 (8R)**, 4948 (2001).
4) G. Srinivasan, E. T. Rasmussen, J. Gallegos, R. Srinivasan, Y. I. Bokhan, and V. M. Laletin: *Phys. Rev. B*, **66**, 029902 (2002).
5) M. Weisheit, S. Fähler, A. Marty, Y. Souche, C. Poinsignon, and D. Givord: *Science*, **315-5810**, 349 (2007).
6) T. Maruyama, Y. Shiota, T. Nozaki, K. Ohta, N. Toda, M. Mizuguchi, A. A. Tulapurkar, T. Shinjo, M. Shiraishi, S. Mizukami, Y. Ando, and Y. Suzuki: *Nature Nanotechnology*, **4**, 158 (2009).
7) Y. Shiratsuchi, T. Fujita, H. Oikawa, H. Noutomi, and R. Nakatani: *Applied Physics Express*, **3-11**, 113001 (2010).
8) T. Ashida, M. Oida, N. Shimomura, T. Nozaki, T. Shibata, and M. Sahashi: *Appl. Phys. Lett.*, **104**, 152409 (2014).
9) X. Qi, H. Kim, and M. G. Blamire: *Philos. Mag. Lett.*, **87**, 175 (2007).
10) K. Sone, H. Naganuma, M. Ito, T. Miyazaki, T. Nakajima, and S. Okamura: *Sci. Rep.*, **5**, 9348 (2015).
11) G. A. Smolenskii and I. E. Chupis: *Sov. Phys.-Usp.*, **25**, 475 (1982).
12) D. H. Wang, W. C. Goh, M. Ning, and C. K. Ong: *Appl. Phys. Lett.*, **88**, 212907 (2006).
13) D. G. Barrionuevo, S. P. Singh, R. S. Katiyar, and M. S. Tomar: *MRS Proceedings*, **1256** (2010).
14) H. Hojo, R. Kawabe, K. Shimizu, H. Yamamoto, K. Mibu, K. Samanta, T. S. Dasgupta, and M. Azuma: *Adv. Mater*, **29**, 1603131 (2017).
15) H. Naganuma, J. Miura, and S. Okamura: *Appl. Phys. Lett.* **93**, 052901 (2008).
16) T. Jia, H. Kimura, Z. Cheng, and H. Zhao: *Sci. Rep.*, **6**, 31867 (2016).
17) H. Hojo, K. Oka, K. Shimizu, H. Yamamoto, R. Kawabe, and M. Azuma: *Adv. Mater*, **30**, 1705665 (2018).
18) D. R. Pelleymounter, D. J. Christie, and B. D. Fries: *57th Annu. Technical Conf. Proc. 2014*, 183 (2014).
19) S. Yoshimura, and M. Kuppan: *Jpn. J. Appl. Phys.*, **57**, 0902B7 (2018).
20) S. Yoshimura, Y. Sugawara, G. Egawa, and H. Saito: *J. Magn. Soc. Jpn.*, **42**, 11 (2008).
21) S. Yoshimura, M. Kuppan: *ITE Technical Report*, **43-15**, 37 (2019).
22) M. Kuppan, D. Yamamoto, G. Egawa, S. Kalainathan, and S. Yoshimura: *Sci. Rep.*, **11**, 11118 (2021).
23) Y. Takeda, S. Yoshimura, M. Takano, H. Asano, and M. Matsui: *J. Appl. Phys.*, **101**, 09J514 (2007).
24) S. Yoshimura, H. Kobayashi, G. Egawa, H. Saito, and S. Ishida: *J. Appl. Phys.*, **109**, 07B751 (2011).

Received Nov. 04, 2021; Accepted Feb. 22, 2022

J. Magn. Soc. Jpn., **46**, 70-75 (2022)

<Paper>

Design of Giant Magnetostrictive Actuator for Ultra-compact EV: Fundamental Consideration on Frequency Characteristics of Magnetostriction Force

T. Kato*, T. Kitamura**, F. Maehara*, H. Nakayama**, K. Ikeda*, A. Endo***, H. Kato****, and T. Narita****

* Course of Science and Technology, Tokai Univ., *4-1-1 Kitakaname, Hiratsuka-shi, Kanagawa 259-1292, Japan*

** Course of Mechanical Engineering, Tokai Univ., *4-1-1 Kitakaname, Hiratsuka-shi, Kanagawa 259-1292, Japan*

*** Department of Electrical Engineering, Fukuoka Institute of Technology, *3-30-1 Wajirohigashi, Higashi-ku, Fukuoka-shi, Fukuoka 811-1295, Japan*

**** Department of Prime Mover Engineering, Tokai Univ., *4-1-1 Kitakaname, Hiratsuka-shi, Kanagawa 259-1292, Japan*

Ultra-compact electric vehicles (EV) have recently begun to be sold instead of general vehicles with gasoline engine to new transportation recently. However, as the outer plate of an ultra-compact EV has low rigidity, the road noise that a tire generates by rotation and the wind noise generated by the projection shape of the vehicle transmit to the inside. It is thought that this interior noise deteriorates ride comfort for passengers. Therefore, we have been investigating a system for actively controlling noise transmitted from the outside with control sound generated by a giant magnetostrictive actuator on the ceiling of the cabin instead of a speaker installed in the vehicle. The control sound forms a wall in the cabin. The giant magnetostrictive actuator is required to produce sufficient thrust, less distortion, and delayed sound waves. In this paper, we studied giant magnetostriction force and performed a frequency analysis on the frequency of the harmonics generated when 100 to 500 Hz of control sound was output.

Keywords: ultra-compact EV, giant magnetostrictive actuator, finite element model, electromagnetic field analysis, road noise, output characteristics, magnetostriction force

1. Introduction

In recent years, the ultra-compact electric vehicle (EV) which is one-or two-seater begins to be sold instead of general vehicles installed gasoline engine to new transportation. Because the ultra-compact EV is a small and wright electric vehicle, it is a characteristic that there is little impact on the environment. Therefore, it is expected that the use of the ultra-compact EV spreads to urban and areas where public transport is not maintained for new transportation tools. However, as the outer plate of the ultra-compact EV has low rigidity, the road noise that a tire generates by rotation and the wind noise to be generated from the projection shape of the vehicle transmits to the inside vehicle. It is thought that this interior noise causes deterioration of the ride comfort for the passenger[1]. In the general vehicle, soundproofing by sound-absorbing materials is installed interior of the vehicle. Furthermore, it is some luxury vehicle has active noise control (ANC) system by control sound generated speaker which is installed in the cabin[2), 3)].

On the other hand, it is difficult to install soundproofing by sound-absorbing materials and ANC system for the ultra-compact EV, because there is a limit to the interior space. The demand for ultra-compact EVs is expected to increase in the future. However, the research and development of noise control systems as noise countermeasures for ultra-compact EVs have not been enough.

We have studied on active control system for transmitted noise from outside by control sound generated by giant magnetostrictive actuator on the wall surface in the cabin instead of vehicle installation speaker[4)-6)]. The features of our proposed system, the control sound form wall surface in the cabin is generated by giant magnetostrictive actuator.

In this system, the output control sound forms the giant magnetostrictive actuator is required sufficient thrust, less distortion, and delay of the sound wave. To maximize the noise reduction performance of the system, it is important to manufacture an actuator that can output signals accurately in the operational frequency range. Therefore, we considered the frequency response of magnetostriction force which is obtained by using electromagnetic field analysis. The magnetostriction force generated a sharp change of giant magnetostrictive material by the magnetic field. In this paper, we studied giant magnetostriction force and frequency analysis of the frequency of the harmonic which was generated when the 100 to 500 Hz which is road noise frequency range[7)-9)] of control sound was output.

2. Design of the giant magnetostrictive actuator considering the output of low frequency control sound

Demand for the ultra-compact EV is expected to increase. However, the ultra-compact EV has urgent issues of countermeasure for lack of comfort by the interior noise. Therefore, we have been studying on new

Corresponding author: H. Kato (e-mail: hkato@tokai-u.jp).

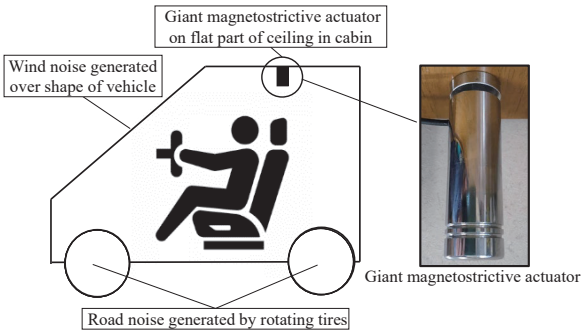

Fig. 1 ANC system for ultra-compact EV using giant magnetostrictive actuator.

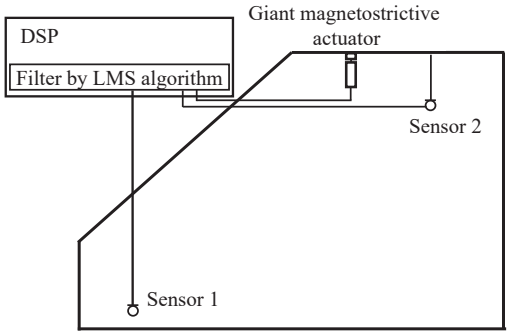

Fig. 2 Schematic of experimental apparatus for noise reduction.

ANC system for the ultra-compact EV for the countermeasure of interior noise by the giant magnetostrictive actuator which is installed on the wall to reduce the impact on inside space and weight of the vehicle as shown Fig. 1. The noise control target of this ANC system is 100 to 500 Hz of the road noise that a tire generates by rotation. This system outputs control sound by the giant magnetostrictive actuator which is installed on the wall in the vehicle. And the value of the sound control effect is muted most at the position of the passenger's ears.

Fig. 2 shows schematic of ANC apparatus. In this system, the condenser microphone is installed under the inside vehicle for measured road noise (Sensor 1) and measured road noise data by Sensor 1 is input to the digital signal processor (DSP). The measured road noise is phase compensated by an adaptive filter using the LMS algorithm and output as a control signal. The control signal is amplified and input to the giant magnetostrictive actuator. And the control sound is output by wall surface vibration using the giant magnetostrictive actuator which is installed on the flat sharped part of the vehicle.

In this ANC system, the noise reduction value at the passenger's ears position (Sensor 2) is effect to sound field in the vehicle consisting of control sound from wall surface vibration by the giant magnetostrictive actuator and road noise transmitted through the vehicle. In addition, the distortion and delay of the output frequency of the giant magnetostrictive actuator influence ANC system quality. In order to increases the noise reduction by ANC, the performance of the giant magnetostrictive actuator that is able to accurately output the signal of the control sound generated by the DSP is important in addition to the output of the control sound for noise and the phase compensation considering the sound field in the vehicle.

In our proposed ANC system, it is necessary to use a highly accurate and output control sound performance giant magnetostrictive actuator to create the ANC system for the ultra-compact EV that is able to noise reduction at the passenger's ears position in the vehicle. In this paper, as a design of the giant magnetostrictive actuator considering the output of low-frequency control sound, an electromagnetic field analysis using a finite element model was performed on the magnetostriction force and frequency characteristics. In this analysis, the frequency of the AC current flowing through the coil was single frequency at the road noise frequency range to be controlled, and we confirmed the distortion of the magnetostriction force.

3. The structure of giant magnetostrictive actuator and magnetostriction force by the giant magnetostrictive material

3.1 The structure of giant magnetostrictive actuator

Fig. 3 shows the structure of the giant magnetostrictive actuator and the dimensions of each part. The giant magnetostrictive actuator is constituted columnar magnetostrictive material, the permanent magnet which is around magnetostrictive material, bobbin, and solenoid coil. The permanent magnet was used to apply a bias magnetic field to magnetostrictive material[10]. Fig. 4 shows the giant magnetostrictive material and coil. The coil was connected AC source and a magnetic field was generated by the current flowing through the coil. The giant magnetostrictive material was stretched by the magnetic field, and the control sound was output by the wall surface generated transmit vibration by the shaft and spring. Other constitution components and materials of the actuator were shown in Table 1.

3.2 The generated magnetostriction force by the current flowing through the coil from the AC source.

Fig. 5 shows the longitudinal direction cut model of the giant magnetostrictive actuator. The permanent magnet which is around the giant magnetostrictive has an N pole on the shaft 1 side and an S pole on the opposite side. In this consideration, the generated giant magnetostriction force on the surface in contact with shaft 2 was a negative value. Because, from Fig. 5, the x axis direction has the origin on the shaft 1 side and the right direction is positive. Therefore, the direction in which the shaft is pushed out by the stretched giant magnetostrictive material is negative. Permanent

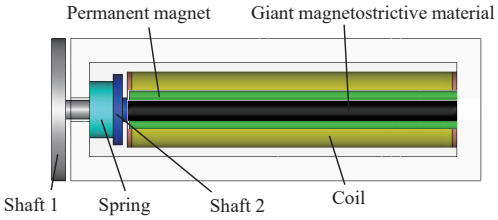

Fig. 3 Internal components of giant magnetostrictive actuator.

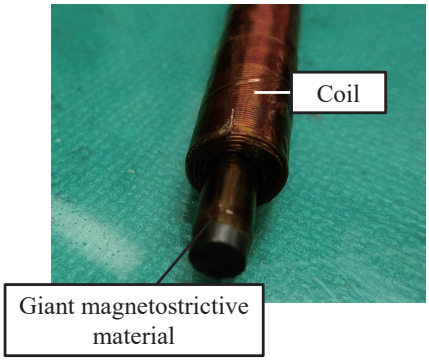

Fig. 4 Giant magnetostrictive material and coil.

Table 1 Details of giant magnetostrictive actuator.

Components	Material	Electrical resistivity [Ωm]
Permanent magnet	Ferrite (FB5B) Neodymium sintered (NEOREC27UX)	-
Shaft 1	Carbon steel	2.1×10^{-7}
Shaft 2	Plastic	-
Coil	Copper	1.7×10^{-8}
Spring	Spring steel	2.1×10^{-7}
Giant magnetostrictive material	Terfenol-D	6.0×10^{-7}

magnets are used as bias magnets in the magnetostrictive actuator. Therefore, the giant magnetostrictive material has magnetostriction force constantly by the effect of the magnetic field from the permanent magnet even though no AC current through the coil. Then, when the AC through the coil, the giant magnetostriction force generated by the constantly working giant magnetostrictive material increases or decreases. And the giant magnetostriction force causes shafts 1 and 2 to transmit the vibration to the wall surface, thereby transmitting the vibration to the wall surface. Outputs sound waves due to vibration.

3.3 Analysis model and material characteristics of the giant magnetostrictive material

In this study, we considered the giant magnetostriction force for output low-frequency control sound using the finite element model of the giant magnetostrictive actuator as shown in Fig. 6 by electromagnetic field analysis by using JMAG Designer Version 16.0 (JSOL Corporation). The giant magnetostrictive actuator output the displacement due to the axial strain of the giant magnetostrictive material. Therefore, the giant magnetostrictive material

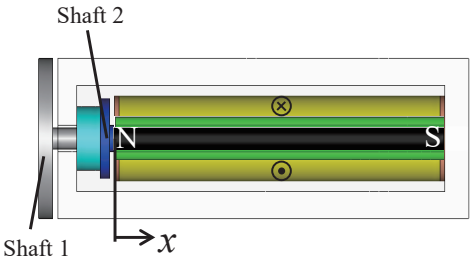

Fig. 5 Direction of magnetostriction force and permanent magnet pole.

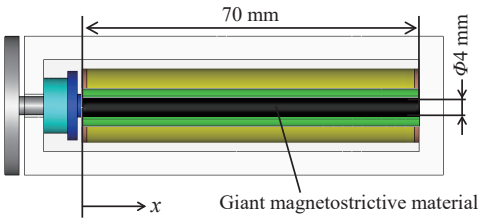

Fig. 6 Size of giant magnetostrictive material by electromagnetic field analysis.

was Terfenol-D with a length of 70 mm and a diameter of 4 mm. And the permanent magnet was magnetized in the axial direction to be applied in the axial direction of the giant magnetostrictive material. There is 0.5 mm air area between the giant magnetostrictive material and permanent magnet. The used coil conductor diameter was 0.5 mm and 201 turns. And the resistance was 2 Ω and inductance was 0. 282 mH.

In this analysis, the material characteristics of giant magnetostrictive material were used value of the magnetic field and magnetic flux density according to research by Sugawara et al[10] as shown Fig. 7 and result of size change by the external magnetic field of magnetostrictive material according to research by Mori[11] as shown Fig. 8. And the young's modulus of giant magnetostrictive material is 26.5 GPa.

In this consideration, we carried out three-dimensional analysis. The number of divided elements was 266855 and the number of nodes was 45689. In the establishment of electromagnetic field analysis, the analysis time increment was 50 μs, the step number was 1000 and the shaft 1 and giant magnetostrictive material were considered eddy current.

4. The consideration of output characteristics by bias magnet materials

Among the elements of the giant magnetostrictive actuator, we considered the giant magnetostriction force and magnetic flux density when the materials of the permanent magnet will be changed by electromagnetic field analysis. The magnetostrictive force from giant magnetostrictive material calculated using Hooke's law by magnetostriction which was calculated magnetic flux density, poisson's ratio, and young's modulus.

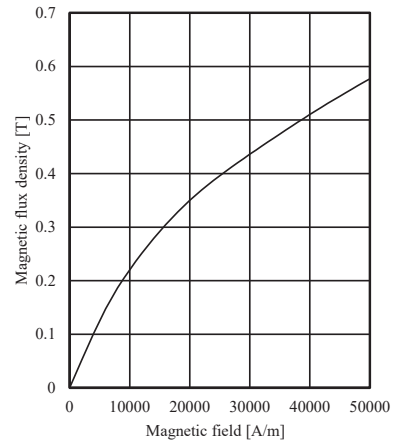

Fig. 7 B-H curve of magnetostrictive material.

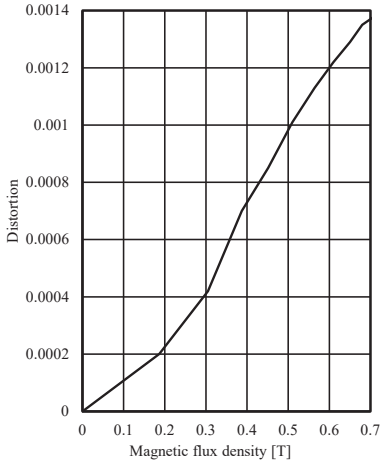

Fig. 8 Relationship between magnetic flux density and distortion.

In this section, we compared the magnetostriction force and magnet flux density of two types of permanent magnets, a ferrite magnet FB5B (0.45 T) and a neodymium sintered magnet NEOREC27UX (1.1 T). Both magnets were manufactured by TDK Corporation. We analyzed magnetostrictive force and magnetic flux density when the AC voltage was changed the frequency applied to the coil from 100 to 500 Hz following road noise frequency band. In this analysis, the sampling frequency was 20 kHz and the voltage amplitude was 3 V.

Fig. 9 shows one of the analysis results of the giant magnetostriction force. In this figure, the red line is a ferrite magnet and the blue line is a neodymium sintered magnet. In this analysis result, the value of magnetostrictive force was negative. Because the *x* axis direction was from the shaft 1 side as the origin and the right direction was positive. From the results, both ferrite and a neodymium sintered magnet have giant magnetostriction force generated by giant magnetostrictive material that stretches and drives the shaft. Compared with the result of ferrite and a neodymium sintered magnet, the magnetostriction force is larger for neodymium sintered magnets, which have a larger residual magnetic flux density value. And, the

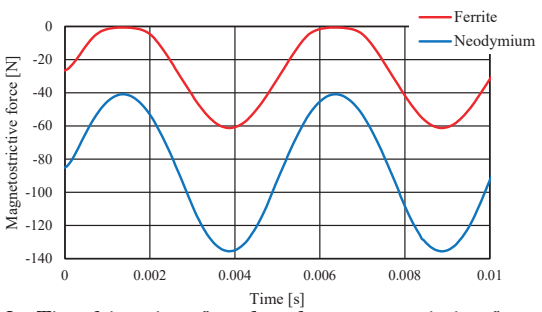

Fig. 9 Time histories of analyzed magnetostriction force of 200 Hz.

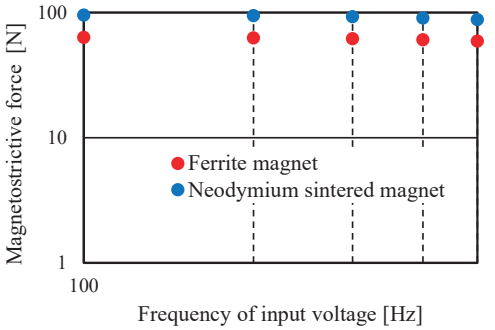

Fig. 10 Magnetostriction force of each frequency.

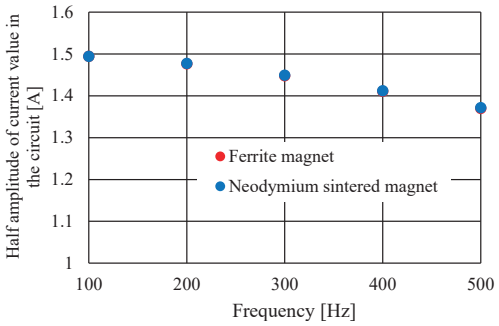

Fig. 11 Half amplitude of current value in the circuit for each frequency.

result of a ferrite magnet, the wave shape was distorted as the magnetostriction force became smaller, and the distortion was larger than the result of the neodymium sintered magnet.

Moreover, Fig. 10 shows both amplitude values of the magnetostriction force at each frequency. From the result, the magnetostriction force was approximately 60 N for ferrite magnets from 100 to 500 Hz. On the other hand, the magnetostriction force was approximately 90 N for neodymium sintered magnets from 100 to 500 Hz.

The Fig. 11 shows the half amplitude of current value in the circuit for each frequency about decrease in the magnetostriction force due to the increase in the frequency of the alternating current. From the Fig. 11, the alternating current value decreases as the frequency increases. Therefore, we considered that the decreases of the magnetostriction force is affected by inductance to voltage in the actuator.

Furthermore, the Fig. 12 shows Average value of iron loss for whole actuator each frequency. From the result, as the frequency increased, the iron loss of the entire

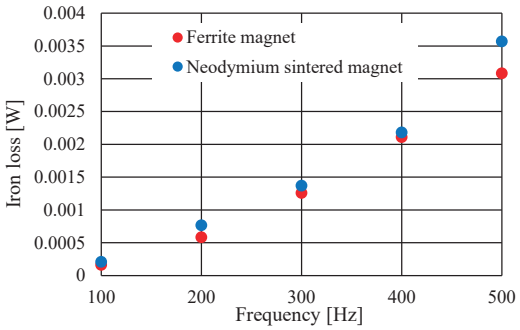

Fig. 12 Average value of iron loss for whole actuator each frequency.

actuator also increased. However, the maximum iron loss value is lower than 0.004 W. Therefore, we considered that the decreases of the magnetostriction force is less impact for iron loss.

5. Spectrum analysis of giant magnetostariction force

In the previous section, we compared the magnetostriction force of two types of permanent magnets, a ferrite magnet, and a neodymium sinteredmagnet. From the result, a ferrite magnet, the wave shape was distorted as the magnetostriction force became smaller, and the distortion was larger than the result of the neodymium sintered magnet. In this section, we considered harmonic wave by spectrum analysis using Fourier transform for the magnetostriction force.

Fig. 13 shows the results of spectrum analysis. From Fig. 11 (a), the frequency of AC is 100 Hz. Therefore, the frequency of the harmonic wave was 200 Hz, 300 Hz, 400 Hz, and 500 Hz in the magnetostriction force. And Fig. 13 (b) to (e), the magnetostriction force has distortion by a harmonic wave as Fig. 13 (a). Moreover, both a ferrite and neodymium sintered magnet has magnetostriction force has distortion by harmonic wave.

Fig. 14 shows the frequency of AC and the single amplitude value of harmonic waves. From the results, the single amplitude value of the magnetostriction force is larger for neodymium sintered magnets, which have a larger residual magnetic flux density value. And, compared with ferrite and neodymium sintered magnet, the neodymium sintered magnet has a smaller single amplitude value of the harmonics. Therefore, it is less distortion in the magnetostriction force. In this investigation, we found that the quality of output sound from the giant magnetostrictive actuator is affected by the bias magnetic field in the actuator.

In our proposed ANC system, when the voltage applied to the giant magnetostrictive actuator becomes large, the harmonics wave of the control sound also becomes large, which may cause a decrease in the noise reduction effect and the sound quality of the masking audio. Therefore, it is important to select to giant magnetostrictive material and a permanent magnet for the development of the giant magnetostrictive actuator for the ultra-compact EV.

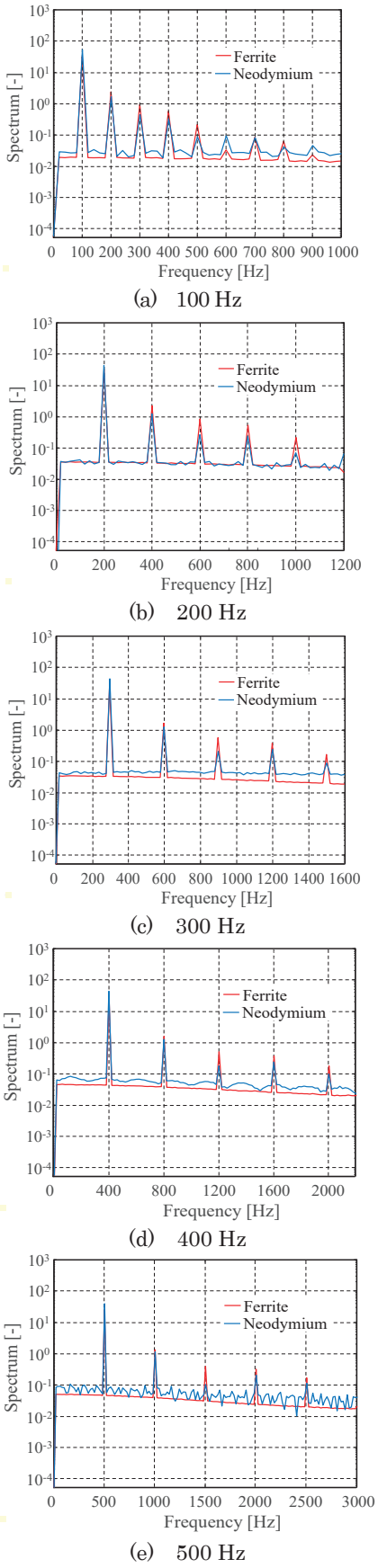

Fig. 13 Spectrum of harmonic wave for each permanent magnet.

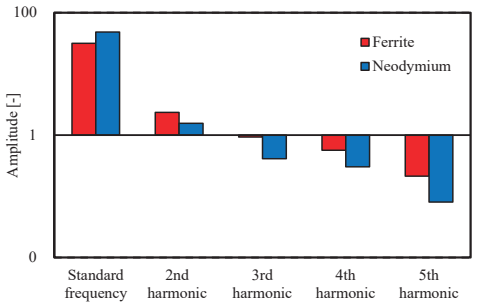

(a) Standard frequency of 100 Hz

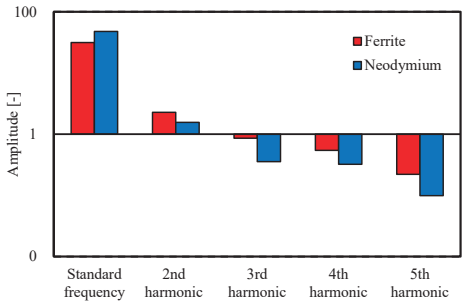

(b) Standard frequency of 200 Hz

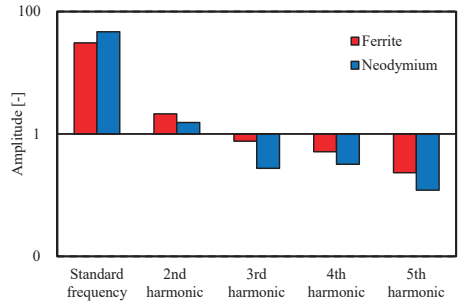

(c) Standard frequency of 300 Hz

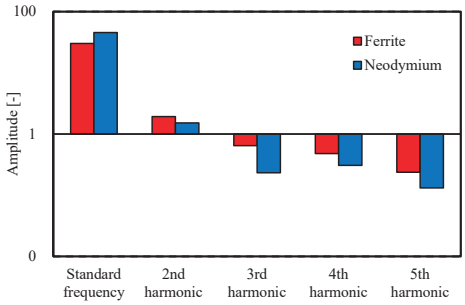

(d) Standard frequency of 400 Hz

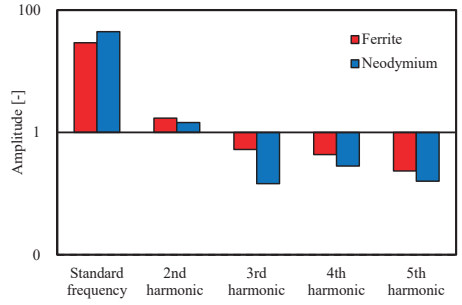

(e) Standard frequency of 500 Hz

Fig. 14 Harmonic wave amplitude for each permanent magnet.

6. Conclusion

In this paper, we studied the characteristics of magnetostriction force which is obtained by using electromagnetic field analysis for the giant magnetostrictive actuator for the ultra-compact EV. We considered the giant magnetostriction force for output low-frequency control sound using the finite element model of the giant magnetostrictive actuator by electromagnetic field analysis and harmonic wave by spectrum analysis for the magnetostriction force.

In this analytical study, we indicated the giant magnetostriction force and magnetic flux density when the materials of the permanent magnet will be changed by electromagnetic field analysis in the elements of the giant magnetostrictive actuator. From the results, the magnetostriction force is larger for neodymium sintered magnets, which have a larger residual magnetic flux density value. And the consideration on the harmonic wave for the magnetostriction force, the neodymium sintered magnet has a smaller single amplitude value of the harmonics. Therefore, it is less distortion in the magnetostriction force. From the results, we found that the quality of output sound from the giant magnetostrictive actuator is affected by the bias magnetic field in the actuator.

In the design of the magnetostrictive actuator, the natural frequency of each element is considered to affect the output characteristics in future. And also, we are changing material with higher magnetic permeability.

Acknowledgements We acknowledge the support of the Japan Keirin Association (JKA), Japan.

References

1) The ministry of land, infrastructure, transport and tourism: *Profits on ultra-compact mobility lead to investigation utilizing experiments*, 63, (2011) (in Japanese).
2) A. Y. Atmojo, Z. Masfuri, M. Sabrina, A. Basuki, Y. Feriadi, Suwarjono, Sugianto: *Journal of Physics Conference Series,* **1951**, (2021).
3) P. N. Samarasinghe, W. Zhang, T. D. Abhayapala: *IEEE Signal Processing Magazine,* **33**, 61, (2016).
4) T. Kato, R. Suzuki, R. Miyao, H. Kato, T. Narita: *Actuators,* **7**, 49 (2018).
5) T. Kato, R. Suzuki, T. Narita, H. Kato, Y. Yamamoto: *IJAEM,* **52**, 153 (2016).
6) T. Kato, T. Kitamura, F. Maehara, H. Nakayama, K. Ikeda, A. Endo, H. Kato, T. Narita: *Trans. Magn. Special Issues,* **5**, 44 (2021) (in Japanese).
7) N. Yukawa: *Trans. Jpn. Mech. Eng.,* **112**, 426 (2009) (in Japanese).
8) D. Flo, D. Pena, L. Pena, V. A. de Sousa Jr., A. Martins: *sensors,* **20**, 2471 (2020).
9) Z. Jia, X. Zheng, Q. Zhou, Z. Hao, Y. Qiu: *sensors*, **20**, 7190, (2020).
10) M. Sugawara and M. Arai: *Trans. Jpn. Soc. Comp. Eng. Sci.,* **7**, 11-080317 (2008) (in Japanese).
11) T. Mori: *J. Robot. Soc. Jpn,* **15**, 334 (1997) (in Japanese).

Received Nov. 08, 2021; Revised Jan. 21, 2022; Accepted Feb. 16, 2022

Journal of the Magnetics Society of Japan

Vol. 46 No. 3 (通巻第321号) 2022年5月1日発行

Vol. 46 No. 3 Published May 1, 2022
by the Magnetics Society of Japan
Tokyo YWCA building Rm207, 1–8–11 Kanda surugadai, Chiyoda-ku, Tokyo 101–0062
Tel. +81–3–5281–0106 Fax. +81–3–5281–0107

Printed by JP Corporation Co., Ltd.
Sports Plaza building 401, 2–4–3, Shinkamata Ota-ku, Tokyo 144–0054
Advertising agency: Kagaku Gijutsu-sha

発行：（公社）日本磁気学会 101–0062 東京都千代田区神田駿河台 1–8–11 東京YWCA会館 207 号室
製作：ジェイピーシー 144–0054 東京都大田区新蒲田 2–4–3 スポーツプラザビル401 Tel.（03）6715–7915
広告取扱い：科学技術社 111–0052 東京都台東区柳橋 2–10–8 武田ビル 4F Tel.（03）5809–1132